Manuscript prepared for Atmos. Chem. Phys.
with version 5.0 of the LaTeX class copernicus.cls.
Date: 18 July 2014

Global free tropospheric NO_2 abundances derived using a cloud slicing technique applied to satellite observations from the Aura Ozone Monitoring Instrument (OMI)

S. Choi[1,2], J. Joiner[2], Y. Choi[3], B. N. Duncan[2], A. Vasilkov[1,2], N. Krotkov[2], and E. Bucsela[4]

[1]Science Systems and Applications Inc., Lanham, MD, USA
[2]NASA Goddard Space Flight Center, Greenbelt, MD, USA
[3]University of Houston, Houston, TX, USA
[4]SRI International, Menlo Park, CA, USA

Correspondence to: S. Choi (sungyeon.choi@nasa.gov)

Abstract. We derive free-tropospheric NO_2 volume mixing ratios (VMRs) by applying a cloud slicing technique to data from the Ozone Monitoring Instrument (OMI) on the Aura satellite. In the cloud-slicing approach, the slope of the above-cloud NO_2 column versus the cloud scene pressure is proportional to the NO_2 VMR. In this work, we use a sample of nearby OMI pixel data from a single orbit for the linear fit. The OMI data include cloud scene pressures from the rotational-Raman algorithm and above-cloud NO_2 vertical column density (VCD) (defined as the NO_2 column from the cloud scene pressure to the top-of-the-atmosphere) from a differential optical absorption spectroscopy (DOAS) algorithm. We compare OMI-derived NO_2 VMRs with in situ aircraft profiles measured during the NASA Intercontinental Chemical Transport Experiment Phase B (INTEX-B) campaign in 2006. The agreement is generally within the estimated uncertainties when appropriate data screening is applied. We then derive a global seasonal climatology of free-tropospheric NO_2 VMR in cloudy conditions. Enhanced NO_2 in the free troposphere commonly appears near polluted urban locations where NO_2 produced in the boundary layer may be transported vertically out of the boundary layer and then horizontally away from the source. Signatures of lightning NO_2 are also shown throughout low and middle latitude regions in summer months. A profile analysis of our cloud slicing data indicates signatures of lightning-generated NO_2 in the upper troposphere. Comparison of the climatology with simulations from the Global Modeling Initiative (GMI) for cloudy conditions (cloud optical thicknesses > 10) shows similarities in the spatial patterns of continental pollution outflow. However, there are also some differences in the seasonal variation of free-tropospheric NO_2 VMRs near highly populated regions and in areas affected by lightning-generated NO_x.

1 Introduction

Tropospheric nitrogen dioxide (NO_2) is mainly produced by fossil fuel combustion, biomass burning, and soil emission near the Earth's surface and by lightning and aircraft emissions in middle and upper troposphere. NO_2 is an important tropospheric constituent, because it is both a pollutant and climate agent. It has adverse effects on human health (Brook et al., 2007) and is one of six criteria pollutants designated by the US Environmental Protection Agency (EPA). It contributes to the formation of ozone, another EPA criteria pollutant. NO_2 also has both direct and indirect radiative effects. The direct effect results from NO_2 absorption of incoming sunlight in the ultraviolet (UV) and visible (VIS) spectral range (e.g., Solomon et al., 1999; Vasilkov et al., 2009). Because NO_2 is an ozone precursor and affects tropospheric concentrations of methane, it also has indirect short- and long-wave radiative effects (e.g. Fuglestvedt et al., 2008; Wild et al., 2001; Shindell et al., 2009).

NO_2 has distinct absorption features in the UV/VIS (primarily at blue wavelengths) that can be remotely sensed by satellite spectrometers using Differential Optical Absorption Spectroscopy (DOAS) techniques. For example, tropospheric vertical column densities (VCDs) of NO_2 have been estimated using spectral radiance measurements from the Global Ozone Monitoring Experiment (GOME) (Richter and Burrows, 2002), SCanning Imaging Absorption spectroMeter for Atmospheric CHartographY (SCIAMACHY) (Richter et al., 2005), the Ozone Monitoring Instrument (OMI) (Boersma et al., 2008, 2011; Bucsela et al., 2006, 2008), and the Second Global Ozone Monitoring Experiment (GOME-2) (Munro et al., 2006). The retrieved tropospheric columns of NO_2 have been evaluated with aircraft, ground-based, and balloon measurements. For example, OMI-derived VCDs show moderately good agreement with aircraft measurements from the NASA Intercontinental Chemical Transport Experiment-A (INTEX-A) and -B (INTEX-B) Experiment (Bucsela et al., 2008; Boersma et al., 2008, 2011), ground-based direct-sun DOAS measurements (Herman et al., 2009), and multi-axis DOAS measurements (Celarier et al., 2008; Hains et al., 2010).

With their global coverage, satellite tropospheric column estimates have provided important information related to tropospheric NO_x chemistry and transport. Satellite retrievals show decreases of NO_2 tropospheric columns over the United States in recent years (Russell et al., 2012; Duncan et al., 2013) and Europe (Castellanos and Boersma, 2012). These reductions result from emission controls and the economic recession. Reductions in NO_2 were also observed over Beijing and the surrounding areas during the 2008 olympic and paralympic games (Witte et al., 2009). Lamsal et al. (2013) showed that OMI-derived surface NO_2 concentrations are highly correlated with urban population, but that the NO_2 to population relationship is geographically dependent. Satellite measurements of tropospheric NO_2 columns have also been utilized to study sources and long range transport of NO_x in conjunction with chemical transport models (e.g., Martin et al., 2003, 2006; Zhang et al., 2007; Beirle et al., 2004, 2011; Jaeglé et al., 2005; Frost et al., 2006; Boersma et al., 2008; Lin et al., 2010; Russell et al., 2010). Top-down approaches using satellite measurements provide NO_x source constraints for regional- and global- scale chemical transport models (Martin et al., 2003; Choi et al.,

2008; Lamsal et al., 2010).

Cloudy data, however, are typically discarded in most studies that use satellite-derived tropospheric NO_2 columns, because clouds screen the near-surface from observation. There have been only a few studies that have utilized cloudy satellite NO_2 observations, and they have primarily focused on lightning-generated NO_x. For example, Boersma et al. (2005) estimated the global lightning NO_x production using GOME cloudy NO_2 measurements. Beirle et al. (2006) also utilized cloudy GOME measurements in combination with US National Lightning Detection Network (NLDN) data to estimate lightning-produced NO_x over the Gulf of Mexico. Indeed, the screening property of clouds can also be exploited to provide unique estimates of NO_2 concentrations in the free troposphere using cloud-slicing techniques. It is otherwise difficult to separate the boundary layer portion of the NO_2 column from the free-tropospheric contribution. Ziemke et al. (2001, 2003, 2005, 2009) pioneered cloud slicing approaches to estimate free tropospheric O_3 concentrations.

Measurements of NO_2 in the free-troposphere are sparse. Aircraft in situ measurements, lidar observations, and balloon-sonde soundings have been confined mainly to field campaigns that are limited in spatial and temporal extents. UV/VIS limb soundings provide vertical profiles of NO_2, but the measurements are limited to the stratosphere (Bovensmann et al., 1999).

Cloud-slicing of NO_2 from satellite measurements can potentially provide additional information about spatial and temporal variations in free tropospheric NO_2 concentrations. Model studies show that lightning NO_x production contributes to free tropospheric NO_2 abundances, but magnitudes and distributions are still largely unknown; in particular, vertical distributions of lightning NO_x are dependent upon the characteristics of the convection parameterizations in the models (Choi et al., 2005, 2008; Allen et al., 2012; Martini et al., 2011). The NO_2 lifetime in the free troposphere (up to a week or more) allows for intercontinental transport of uplifted anthropogenic and lightning-generated NO_2 (e.g., Li et al., 2004; Wang et al., 2006; Zhang et al., 2008; Walker et al., 2010). While this transport has been simulated, global NO_2 observations in the free troposphere have not been available for extensive evaluation. In addition, knowledge of the distributions of NO_2 in the free troposphere is important for calculations of its anthropogenic radiative forcing (e.g. Fuglestvedt et al., 2008; Wild et al., 2001; Shindell et al., 2009).

In this study, we use OMI to infer free tropospheric NO_2 VMR. To derive this quantity, we use the OMI-inferred above-cloud NO_2 columns and cloud parameters from highly cloudy scenes. We evaluate the derived OMI NO_2 VMRs with available aircraft data from the NASA INTEX-B campaign. We derive a global seasonal climatology of free tropospheric NO_2 VMRs from OMI. For reference, we show an example of a comparison with NO_2 fields simulated by a chemical-transport model, the Global Modeling Initiative (GMI). We also construct coarse profiles for several regions with sufficient cloud pressure variability.

2 Data description

2.1 Space-based measurements from OMI

OMI is a UV/VIS grating spectrometer that flies aboard the NASA Aura spacecraft (Levelt et al., 2006). Aura is in a sun-synchronous orbit with a local equator crossing time of 13:35 ± 0:05 (ascending node). OMI provides daily global coverage with a nadir pixel size of approximately $13 \times 24\,\mathrm{km}^2$ and a swath width of about $2600\,\mathrm{km}$. It has separate channels for UV and VIS observations. The OMI spectral resolutions in the VIS and UV channels are 0.63 and 0.45 nm, respectively. An obstruction outside the instrument (known as the "row anomaly") has reduced the swath coverage starting in May 2008. In order to avoid the row anomaly, we focus on OMI data obtained from 2005–2007.

2.1.1 OMI cloud scene pressure

OMI has two independent cloud retrieval algorithms. They are described in detail by Stammes et al. (2007). Here, we provide a brief explanation of these algorithms. One algorithm uses the collision-induced O_2-O_2 absorption band near 477 nm in the VIS channel; its official product name is OMCLDO2 (Acarreta et al., 2004; Sneep et al., 2008). The other makes use of the filling-in effect of rotational Raman scattering (RRS) at wavelengths from 345 to 354 nm in the UV-2 channel (OMCLDRR) (Joiner and Vasilkov, 2006; Vasilkov et al., 2008).

Both algorithms use the Mixed Lambertian Equivalent Reflectivity (MLER) model that accurately reproduces the observed Rayleigh scattering or atmospheric absorption in a cloudy scene (Koelemeijer and Stammes, 1999; Ahmad et al., 2004). The MLER model utilizes the independent pixel approximation; it treats a measured cloudy pixel radiance (I_m) as a weighted sum of two independent subpixels: clear (I_clr) and cloudy (I_cld). The clear and cloudy subpixels are weighted by an effective cloud fraction (f_c), i.e.,

$$I_\mathrm{m} = I_\mathrm{clr}(p_\mathrm{terrain}) \cdot (1 - f_\mathrm{c}) + I_\mathrm{cld}(p_\mathrm{c}) \cdot f_\mathrm{c}, \quad (1)$$

where p_terrain is the terrain pressure and p_c is the cloud optical centroid pressure (OCP); p_c can be considered as a reflectance-weighted pressure located inside a cloud (Vasilkov et al., 2008; Joiner et al., 2012). This is distinct from the cloud-top pressure derived from thermal infrared measurements. To model I_cld and I_clr, clouds and the Earth's surface are treated as Lambertian reflectors (i.e., through which no light is transmitted). For the clear-sky contribution, the surface LER is taken from a precomputed climatology that varies in space and time. The Lambertian clouds are treated as having a fixed albedo of 0.8. In scenes containing transmissive clouds with an overall LER < 0.8, $f_\mathrm{c} < 1$; the clear subpixel contribution (first term in the right-hand side of Eq. 1) accounts for light transmitted through the cloud. We also note that f_c is different from the geometric cloud fraction as it is designed to account for cloud transmission within the context of the MLER model. We have found that f_c is practically spectrally invariant over the UV/VIS wavelengths considered here. In the

OMCLDRR algorithm, f_c is retrieved by inverting Eq. (1) at a wavelength unaffected by RRS. Then p_c is retrieved to be consistent with the observed amount of RRS filling-in.

We also make use of a wavelength-dependent quantity known as the cloud radiance fraction (f_r), defined as the fraction of radiance contributed by clouds (and aerosol). Within the context of the MLER model, f_r is computed as

$$f_r = \frac{I_{cld}(p_c) \cdot f_c}{I_m}. \quad (2)$$

Acarreta et al. (2004) and Vasilkov et al. (2008) used radiative transfer calculations to estimate errors of OMI cloud OCPs. They estimate that errors should be in the range 50 hPa or less for a wide range of viewing condition and for moderate to high cloud effective fractions (or cloud optical thicknesses). Comparison of the two retrievals (OMCLDRR and OMCLDO2) has been used as a means to evaluate the retrieved cloud pressures after the launch of Aura OMI and may provide an upper limit on the errors (Sneep et al., 2008; Joiner et al., 2012). For effective cloud fractions > 0.75, the mean differences are 40 hPa (OMCLDO2 having higher pressures on average) over land and 25 hPa over ocean and standard deviations are approximately 63 hPa over both land and ocean (Joiner et al., 2012). Cloud OCPs from OMCLDO2 and OMCLDRR are very similar, particularly for pixels with high values of f_c and f_r (Joiner et al., 2012). However, there are some subtle differences, particularly over the Pacific where there is a high incidence of multi-layer clouds. As a result, cloud slicing NO_2 VMRs derived with the two cloud products exhibit some differences in spatial patterns, particularly over equatorial pacific and Gulf of Mexico. In this work, we use p_c from OMCLDRR. For reference, we show sample results that use OMCLDO2 p_c in Appendix D2.

2.1.2 OMI above-cloud and tropospheric column NO_2

NO_2 slant column densities (SCD) are retrieved from solar backscattered radiances in the VIS channel with a spectral fitting window of 405–465 nm. These data are provided in the OMNO2A product (Boersma et al., 2011). Fitting errors of NO_2 SCDs range from 0.3–1 $\times 10^{15}$ cm^{-2}. There is evidence that NO_2 SCDs are positively biased (Krotkov et al., 2012; Boersma et al., 2014) which may lead to a high bias in NO2 VCD of 4–5$\times 10^{14}$ cm^{-2} (Boersma et al., 2014; Belmote Rivas et al., 2014). The effect of this bias on our results is not yet clear. We plan to reprocess the OMI data when a new version of OMI SCDs is released.

We calculate air mass factors (AMFs) for highly cloudy conditions, assuming scattering clouds with a large total optical depth uniformly distributed over a 1 km layer (near-Lambertian clouds) that provides the same cloud OCP as retrieved from OMCLDRR. Henceforth we refer to this AMF as the "near-Lambertian cloudy AMF". We divide the OMI NO_2 SCDs by the near-Lambertian AMFs to obtain estimates of NO_2 VCDs in such highly cloudy conditions. The cloudy AMF formulation is discussed in further detail in Sect. 3.2.

It is useful at this point to introduce the concept of cloud scene pressure (p_{scene}) given by

$$p_{\text{scene}} = f_{\text{r}} \cdot p_{\text{c}} + (1 - f_{\text{r}}) \cdot p_{\text{terrain}}. \quad (3)$$

The derived $\mathrm{NO_2}$ VCD in a cloudy pixel can be interpreted as the total column from p_{scene} to the top-of-the-atmosphere (i.e., the total column above p_{scene}), assuming that the $\mathrm{NO_2}$ profile is vertically uniform between p_{terrain} and p_{c} (Joiner et al., 2009). Because this condition will not be met for $\mathrm{NO_2}$ in highly polluted regions, here we use only pixels where $f_{\text{r}} > 0.9$. For these pixels, the below-cloud contribution to the observed VCD (i.e., from the second term on the right hand side of Eq. 3) is small and $p_{\text{scene}} \simeq p_{\text{c}}$. Like p_{c}, p_{scene} is located below the physical cloud top altitude. Henceforth we refer to the derived $\mathrm{NO_2}$ VCD in a cloudy scene ($\mathrm{NO_2}$ VCD = $\mathrm{NO_2}$ SCD/$\mathrm{AMF_{geometric}}$) as the above-cloud $\mathrm{NO_2}$ VCD.

2.2 $\mathrm{NO_2}$ in-situ measurements from NASA DC-8 aircraft during INTEX-B

We evaluate OMI $\mathrm{NO_2}$ cloud slicing results using INTEX-B aircraft in situ $\mathrm{NO_2}$ measurements. INTEX-B was an atmospheric field campaign conducted in the spring of 2006. Its major goals included (1) understanding transport and evolution of Asian pollution and its implications for air quality, and (2) validating space-borne retrievals of tropospheric composition including those from OMI (Singh et al., 2009). INTEX-B $\mathrm{NO_2}$ data were obtained using the University of California at Berkeley Laser-Induced Fluorescence instrument (TD-LIF) on the NASA DC-8 aircraft in 1 s intervals (Thornton et al., 2000; Perring et al., 2010; Bucsela et al., 2008). At 1 Hz, the mixing ratio observations have precisions ranging from $\pm 23\ \mathrm{pptv}$ at 1000 hPa to $\pm 46\ \mathrm{pptv}$ at 200 hPa at a signal to noise ratio of 2.

2.3 GMI model simulation

We use GMI chemical transport model simulations for comparison with our $\mathrm{NO_2}$ cloud slicing results. A detailed model description is provided in Duncan et al. (2007) and Strahan et al. (2007). Here, we provide a brief explanation of the model. The model is driven by Goddard Earth Observing System 5 (GEOS-5) meteorological fields (Rienecker et al., 2011). The GMI spatial resolution is 2° latitude $\times$ 2.5° longitude. The GMI vertical extent is from the surface to 0.01 hPa, with 72 levels; vertical resolution ranges from $\sim 150\ \mathrm{m}$ in the boundary layer to $\sim 1\ \mathrm{km}$ in the free troposphere and lower stratosphere. Model outputs are sampled at the local time of the Aura overpass.

The GMI chemistry combines stratospheric chemical mechanisms (Douglass et al., 2004) with detailed tropospheric $\mathrm{O_3}$-$\mathrm{NO_x}$-hydrocarbon chemistry that has its origins in the Harvard GEOS-Chem model (Bey et al., 2001). In addition to chemistry, the model includes various emissions sources, aerosol microphysics, deposition, radiation, advection, and other important chemical and physical processes including lightning $\mathrm{NO_x}$ production (Allen et al., 2010).

In this study, we extract GMI $\mathrm{NO_2}$ concentrations/burdens for three different sets of conditions.

(1) tropospheric NO_2 VMRs for heavily cloudy conditions (cloud optical thickness $\tau > 10$), (2) tropospheric NO_2 VMRs for all-sky conditions, and (3) lightning contribution to the tropospheric NO_2 VMRs. The estimated contribution of lightning to tropospheric NO_2 is obtained by subtracting a no-lightning run from the full run with lightning for highly cloudy conditions (cloud optical depth > 10). Although we henceforth refer to this quantity as the lightning NO_2 contribution, we note that complex, non-linear chemical feedbacks between NO_x, O_3, and other chemically-active constituents in upper troposphere occur; therefore, this quantity should not be strictly interpreted as an exact lightning NO_2 contribution. For example, we obtain some negative values at northern high latitudes during the Dec.-Feb. period (bottom right panel of Fig. 7 in Sect. 4.2). For comparison with OMI cloud slicing tropospheric VMRs, we average the GMI NO_2 VMRs over the appropriate OMI scene pressure range.

3 Cloud slicing technique

3.1 General approach

The cloud slicing technique takes advantage of optically thick clouds to estimate a VMR of a target trace gas in the free troposphere between the clouds (Ziemke et al., 2001, 2003). We infer NO_2 VMRs using the slope derived from linearly fitting the collocated OMI above-cloud column NO_2 to cloud scene pressures. Figure 1 illustrates a simple example of this technique (not to scale). We require at least two nearby above-cloud NO_2 VCDs for different cloud scene pressures as in Fig. 1a. The two OMI measurements are shown in a pressure-VCD coordinate plane in Fig. 1b. NO_2 VCD (VCD_{NO_2}) between the two pressure levels p_1 and p_2 ($p_1 < p_2$) can be derived by integrating the NO_2 VMR (VMR_{NO_2}) over pressure from p_1 to p_2, i.e.,

$$\mathrm{VCD}_{\mathrm{NO_2}}{}_{p_1}^{p_2} = \frac{R_{\mathrm{air}}}{k_B g} \times \int_{p_1}^{p_2} \mathrm{VMR}_{\mathrm{NO_2}}(p)\, dp, \tag{4}$$

where R_{air} is the gas constant, k_{B} is the Boltzmann constant, and g is the gravitational acceleration. Assuming a constant mixing ratio over the range p_1 to p_2 in Eq. (4), the mean NO_2 VMR in this pressure interval is given by

$$\mathrm{VMR}_{\mathrm{NO_2}} = \frac{\Delta \mathrm{VCD}}{\Delta p} \frac{k_B g}{R_{\mathrm{air}}}. \tag{5}$$

From this relationship, the NO_2 VMR in the pressure range of OMI cloud measurements is proportional to the fitted slope of NO_2 VCD versus cloud scene pressure, as shown in Fig. 1c. The confidence interval of NO_2 VMR also can be derived from the linear fit if more than two observations are available. In Fig. 1c, we show the pressure range of the NO_2 VMR (vertical error bar) as well as the confidence interval (horizontal error bar).

By assuming a uniform free tropospheric NO_2 VMR within the OMI-observed cloud pressure range, we limit the number of retrieved parameters to 2 (slope and y-intercept, related to free-

tropospheric VMR and stratospheric VCD, respectively). This simplifies the retrieval and its error analysis. We note that this assumption is only used for the linear fitting. The uniform VMR assumption here is independent of NO_2 profile assumptions used in the AMF calculation, since the above-cloud VCDs are derived prior to this step.

While the cloud slicing technique derives the free tropospheric NO_2 VMR without the need for a prescribed stratospheric column or other a priori information, it relies on several assumptions and conditions. The method works well only with a relatively large number of nearby cloudy OMI pixels that have a sufficient variation in cloud pressure. We also note that the derived NO_2 VMR information is based on the assumption that NO_2 is vertically and horizontally well mixed in the given pressure range and spatial extent of the OMI pixel collections. In addition, we assume that the stratospheric column remains constant during the time period and over the area of the OMI pixel sample. Finally, the absolute magnitudes of the derived tropospheric mixing ratios and stratospheric columns are only as accurate as the above-cloud NO_2 VCDs. Errors in the derived cloud scene pressures may contribute additional uncertainty. It should also be noted that the NO_2 VMRs are derived in highly cloudy conditions. These conditions may not be representative of the general all-sky atmosphere.

In order to ensure that appropriate data are used for cloud-slicing, we apply rigorous data filtering criteria. This results in the use of approximately 10–15 % of the available pixel data depending on season and geolocation. The data selection criteria are summarized in Table 1 and discussed in detail in Appendix A1.

Although we show a case of two adjacent OMI measurements in Fig. 1 for simplicity, we typically use an OMI pixel collection that consists of a number of nearby measurements collected over one OMI orbit; this minimizes the effects of random errors from both the above-cloud OMI NO_2 VCD and p_{scene}. Examples are discussed in detail in Sect. 4.1. The detailed methodology used to obtain the seasonal climatologies is explained in Appendix A2 and Sect. 4.2.

3.2 Formulation of cloudy AMF and comparison of NO2 VMRs derived using near-Lambertian and geometric AMFs in complex (realistic) cloudy conditions

In this subsection, we describe how we formulate the near-Lambertian cloudy AMF and attempt to assess potential errors in our approach owing to various AMF assumptions. To do this, we first simulate OMI cloud and slant column measurements in realistic cloudy conditions using the LInearized Discrete Ordinate Radiative Transfer (LIDORT) model (Spurr et al., 2001). For these simulations, we use the the C1 water-droplet cloud model with a modified-gamma size distribution and the maximum radius is 15 μm (Diermendjian, 1964, 1969; Ahmad et al., 2004). All calculations are performed at 440 nm. Similar calculations were performed at shorter UV wavelengths by Ziemke et al. (2009).

We then retrieve VMRs based on the near-Lambertian cloudy AMF assumption (i.e., scattering cloud with a large total optical depth uniformly distributed over a thin layer). Previous radiative transfer studies have shown that there is enhanced scattering and absorption (e.g., of NO_2) within and above bright clouds (Hild et al., 2002; Eskes and Boersma, 2003; Boersma et al., 2005; Beirle et al., 2006, 2009; Ziemke et al., 2009). A near-Lambertian AMF may be a reasonable AMF formulation to use in a cloud-slicing approach. We also examine the use of the geometric AMF ($AMF_{geometric} = \sec(SZA) + \sec(VZA)$, where SZA and VZA are the solar and view zenith angles, respectively) for determining free-tropopsheric NO_2 mixing ratios. $AMF_{geometric}$ is appropriate for use in an atmosphere where the effects of Rayleigh scattering are relatively small. This is generally the case for highly cloudy observations at NO_2 wavelengths at moderate SZAs. For example, tropospheric O_3 columns and VMRs derived with the geometric AMF assumption at shorter wavelengths have been validated by comparisons with ozonesondes (Ziemke et al., 2003) and other in situ data (Avery et al., 2010).

In order to accurately simulate OMI measurements, we first need a realistic NO_2 profile. Here, we use a C-shaped profile generated by the GMI model in polluted conditions as shown in Fig. 2a. We also need to use realistic cloud optical depth (COD) profiles. A combination of CloudSat/MODIS data (i.e., the CloudSat 2B-TAU product) provides a source of such data (CloudSat, 2008). Examples of COD profiles are shown in Fig. 2b (solid lines). The red solid line in Fig. 2b shows a Gaussian-like COD profile where the reported collocated OMI cloud optical centroid pressure (OCP, see Sect. 2.1.1) was 656 hPa. The blue line shows another example of a multi-layer vertically-extended cloud. These profiles are from a tropical deep convective complex and were also used in the study of Vasilkov et al. (2008); the OMI cloud radiance fractions are greater than 0.9 for these cases. Figure 2c shows the corresponding scattering weights (solid lines) for these cloud profiles. For both cases there is enhanced weighting in the top portion of the cloud with decreasing weights in the bottom portions. The calculations were performed at SZA=46° at nadir.

Without a priori knowledge of the COD profile (which is the case in general) and with only a single retrieved OMI cloud OCP value for each observation, we must make simplifying assumptions in order to compute scattering weights. For the near-Lambertian approach, we assume that the COD profile is uniform and optically thick (total COD=25) within a thin layer (1 km geometrical thickness). The dotted lines in Fig. 2b show such clouds that would produce the observed OMI cloud OCP. The scattering weights corresponding to these uniform profiles are shown in Fig. 2c (dotted lines). Although the scattering weights from the uniform clouds show slightly enhanced scattering above the cloud OCP (including both the very top portion of the cloud as well as above the physical cloud top), they do not reproduce the shape of the scattering weights from the CloudSat optical depth profiles.

Figure 3a shows near-Lambertian COD profiles at different cloud OCPs. The corresponding scattering weights for these clouds are shown in Fig. 3b along with geometric weighting functions; the

latter assumes uniform weighting related to the viewing geometry (i.e., sec(SZA)+sec(VZA), where SZA and VZA are the solar and viewing zenith angles, respectively) above the cloud OCP with zero weighting below. The overall shape of the scattering weights for near-Lambertian clouds does not vary much with cloud OCP; however the amount of enhanced scattering above and inside the cloud depends upon the cloud OCP.

We next compute (1) near-Lambertian AMFs and (2) geometric AMFs using our scattering weight calculations and the C-shaped and uniform a priori profiles. We integrate the a priori profiles using the scattering weights to obtain a priori SCDs, and then divide the a priori SCDs by a priori above-cloud VCDs (integrated from the OMI cloud pressure to the top of the atmosphere without weighting) to produce cloudy AMFs. The difference between above-cloud NO_2 VCDs computed using near-Lambertian and geometric AMFs varies with the viewing geometry, cloud OCP, and a priori NO_2 profile. Above-cloud NO_2 VCDs from the geometric AMFs are larger than those from the near-Lambertian AMFs in most viewing geometries, except where the solar zenith angles are greater than $\sim 70^\circ$. In moderate viewing geometries (SZA$<70^\circ$), the differences are larger when the cloud OCP is greater (low clouds). The VCDs computed using the geometric AMFs are higher than with near-Lambertian AMFs by up to maxima of 5% (14%) for the C-shaped (uniform) NO_2 profiles. For the remainder of this section and in appendices, we focus on results using near-Lambertian AMFs with the C-shaped NO_2 profile.

We next simulate SCDs for 10 different cloud optical depth profiles from CloudSat/MODIS using LIDORT at nadir and SZA=46° for the C-shaped NO_2 profile in Fig. 2a. Figure 4a and b shows the simulated above-cloud VCDs derived using near-Lambertian and geometric AMFs, respectively, versus the corresponding cloud OCPs. We then derive NO_2 VMRs from the slopes for these two AMFs. The derived NO_2 VMRs, 95% confidence interval, and the true NO_2 VMR are presented.

The errors in derived NO_2 VMRs are similar for both AMF assumptions; errors are in the range 20-30% with a somewhat higher error and larger confidence interval for the geometric AMF assumption. The two points deviating from the others in the near-Lambertian AMF scenario result from multi-layer clouds. Overall, the use of the near-Lambertian cloudy AMF gives slightly more accurate NO_2 VMR than the geometric AMF.

In addition to the error owing to the near-Lambertian COD assumption, NO_2 a priori profile shape can be another source of error in the derived VMRs. Especially for situations with outflow of lightning or convective transport of boundary layer pollution to high altitudes, the profile will be different from the C-shaped profile used in the near-Lambertian AMF calculation. It is difficult to obtain realistic a priori profiles for such situations from current chemical transport models owing to uncertainties in simulating NO_2 vertical transport and in the lightning NO_x production. Consequently, our results in these situations may contain additional errors owing to incorrect NO_2 profile shape assumptions.

In the remainder of this paper, we show results based on the near-Lambertian cloudy AMF and

with the C-shaped a priori profile. We show sample results derived with geometric AMFs in Append. D1. In brief, the results derived using both AMFs display similar spatial and seasonal variability, although the NO_2 VMR magnitudes are somewhat smaller using the near-Lambertian AMFs. We note that the near-Lambertian AMF produces results closer to the in-situ data (Fig. 6 in Sect. 4.1) and the GMI model (Fig. 7 in Sect. 4.2). However, the global seasonal climatology derived using near-Lambertian AMF shows some negative values. For example, values of around -10 pptv are seen over southern middle to high latitudes (latitudes>40°S) during the Dec.-Feb. period (upper right panel of Fig. 7 in Sect. 4.2). The results using the geometric AMF show small positive values in these areas. More discussion on these differences is provided in Appendix D1.

4 Results and discussions

4.1 Evaluation of OMI NO_2 VMR with INTEX-B data

In this section, we evaluate OMI NO_2 VMRs derived from cloud slicing using aircraft in situ NO_2 measurements made during INTEX-B. For individual comparisons, we use OMI pixel collections from a single orbit that must have occurred within 2 days of an aircraft measurement. Furthermore, the absolute value of the difference in the time of day between the aircraft and satellite measurements must be < 5 h. We use relatively relaxed temporal collocation criteria (different days for OMI and INTEX-B NO_2 measurements) because most of the aircraft column measurements (from aircraft spirals) are made in clear conditions (Singh et al., 2009) while cloud slicing from OMI requires highly cloudy conditions.

To meet the spatial collocation requirements, OMI pixels must be within a box of 8° latitude × 10° longitude, centered at the location of each INTEX-B profile; we use this relatively large box to ensure the availability of an adequate number of OMI cloudy pixels. If we have multiple OMI pixel collections from adjacent days for a single aircraft profile, we average the derived VMRs from all applicable collections. Even with these relatively relaxed collocation criteria, we obtained matchups in only a few areas.

Figure 5 shows examples of cases of reasonably good agreement (within the calculated uncertainties) between OMI cloud slicing and INTEX-B NO_2 VMR. For each row, the first column shows the collection of above-cloud NO_2 columns and cloud scene pressures (light blue dots) and the fitted slope (black line) with the date of the OMI measurement, similar to Fig. 1b. Here, Δt refers to the aircraft minus OMI time differential. The second column, similar to Fig. 1c, shows the OMI cloud slicing NO_2 VMR marked by a square in the same color as used in the first column (light blue). The vertical error bar represents the applicable OMI cloud scene pressure range, and the horizontal error bar is the 95 % confidence interval of the retrieved VMR.

Also shown are the collocated INTEX-B NO_2 profiles (dark blue lines) with the corresponding standard errors of the mean (gray shaded areas) and the date of the DC-8 aircraft measurement. We

also show the average of the INTEX-B NO_2 VMR over the OMI cloud scene pressure range (dark blue square). The vertical and horizontal error bars represent the pressure range and the standard error of the mean for the INTEX-B measurements, respectively. This standard error of the mean (blue horizontal error bar) is smaller than that of the profiles (gray shaded area), as more VMR measurements are averaged. The third column shows the location of OMI pixels and INTEX-B profiles (in the same colors as used in the first and the second columns).

The top row of Fig. 5 shows an example of NO_2 observations over a populated area. The INTEX-B profile was measured near Houston, TX on 19 March 2006. OMI cloudy observations were made on the same day. According to the flight report, this flight segment was affected by clouds; thus this is one of the very few cases when cloudy aircraft measurements coincide with OMI cloud slicing results. The INTEX-B free tropospheric NO_2 profile is fairly uniform for $p < 880\,\mathrm{hPa}$, while the profile shows a sharp vertical gradient for $p \gtrsim 900\,\mathrm{hPa}$. We use only OMI pixels with $p_{\mathrm{scene}} < 900\,\mathrm{hPa}$, thereby avoiding pixels affected by the sharp NO_2 profile gradient. The retrieved OMI VMR agrees moderately well with the INTEX-B profile for this case (OMI minus INTEX-B difference of $\sim$-2.7 pptv or -7.4 %).

The bottom row in Fig. 5 shows an example for a clean oceanic region, measured over the north-east Pacific on 8 May 2006. The INTEX-B profile has a significantly lower average NO_2 VMR, and the profile is nearly uniform throughout the measured pressure range. There are no surface NO_x emission sources in this region, and there is no evidence of a significant elevated NO_2 pollution plume. The OMI above-cloud column NO_2 has higher values than in the Houston case at 30° N in March, presumably because the stratospheric column NO_2 is higher in this Pacific case at 45° N in May, giving a higher baseline value to the above-cloud columns. The retrieved OMI NO_2 VMR has a large confidence interval as a result of the large scatter in the above-cloud OMI NO_2 column. Nevertheless, the obtained OMI NO_2 VMR and the INTEX-B NO_2 profile agree moderately well (OMI minus INTEX-B difference $\sim$-8.7 pptv or -48 %).

Although there are several examples of relatively good agreement as shown in Fig. 5, there are also a number of cases with significant discrepancies. There may be several reasons these differences. Firstly, the INTEX-B NO_2 profiles were obtained in relatively cloud-free conditions (except for a few cases including the 19 March 2006 profile shown in Fig. 5). Cloud conditions may alter NO_x-O_3 photochemistry; this poses an intrinsic problem for the comparison. Spatial and temporal variability of tropospheric NO_2 also contribute to differences between aircraft and satellite data given the relaxed collocation criteria. We show examples of discrepancies between OMI and aircraft data in Appendix B.

Figure 6 summarizes all comparisons between OMI and INTEX-B NO_2 VMRs. We analyzed all successful collocations of INTEX-B profiles and OMI cloud slicing NO_2 VMRs and produced a scatter diagram in the left panel of Fig. 6. The vertical error bars are the 95 % confidence intervals of OMI NO_2 VMRs, and the horizontal error bars are the standard error of the mean of INTEX-

B NO_2 VMRs. The INTEX-B standard error of the mean is small ($\lesssim 3$ pptv) as compared with the magnitude of the NO_2 VMR, except for two cases that deviate significantly from the $1:1$ line (~ 6 pptv) marked in red color in the left panel of Fig. 6. The locations of the INTEX-B profiles are presented in the right panel of the Fig. 6, with high standard error cases marked in red. The left panel using all the matchups shows significant scatter; the root mean square (RMS) of the difference is $\simeq$ 50 pptv and the OMI minus INTEX-B mean difference is $\sim$-16 %. OMI and INTEX-B VMRs do not show any correlation. However, if we remove the INTEX-B profiles with high standard errors, OMI and INTEX-B VMRs exhibit a weak correlation ($R = 0.2$) and the scatter is slightly reduced (RMS differences $\simeq$ 45 pptv). The mean difference between the OMI and the INTEX-B VMR is $\sim$9 % in this case.

Overall, this comparison, even with its intrinsic limitations, provides some confidence in the ability to estimate NO_2 mixing ratios with OMI cloud slicing.

For comparison between OMCLDRR and OMCLDO2 results, a scattergram using OMI VMRs derived with OMCLDO2 cloud data is presented in Appendix D2. OMCLDO2 results show similar magnitudes and scatter as compared with OMCLDRR. When we exclude the high standard error cases, OMCLDO2 data result in slightly higher scatter and lower correlation versus INTEX-B.

4.2 Global seasonal climatology of free tropospheric NO_2 VMR

We construct a seasonal climatology of OMI free tropospheric NO_2. Details regarding the construction of the climatology are provided in Appendix A2.

In analyzing the global climatology, we focus on spatial and temporal variations of the NO_2 VMR rather than its absolute magnitude. In this section, we examine aspects of the OMI free tropospheric NO_2 climatology in the context of anthropogenic and lightning contributions. We also show GMI free tropospheric NO_2 VMRs for comparison.

We use the standard error as an estimate of uncertainty for the derived NO_2 climatology; this assumes that the error of the derived NO_2 VMR has zero mean and that errors for individual measurements are random and uncorrelated with respect to each other. While these assumptions are not likely to strictly hold (there are indications of a bias), they may lead to reasonable uncertainties with respect to the derived spatial and temporal patterns. We show the NO_2 VMR climatology where the standard error < 10 pptv (if VMR < 20 pptv) or 50 % (if VMR > 20 pptv). For more details regarding quality assurance, see Appendix C. In addition to the standard errors, we present auxiliary data to help interpret the climatology, including the number of measurements, confidence intervals, standard deviations, and the mean cloud scene pressures corresponding to the NO_2 climatology in Fig. C1 of Appendix C.

Figure 7 shows global data averaged over June–August (left column) and December–February (right column) for 2005–2007. The first row shows the OMI-derived 3 month seasonal climatology of free tropospheric NO_2 VMRs. The second row displays the GMI NO_2 VMRs in cloudy ($\tau > 10$)

conditions, averaged over the corresponding OMI cloud scene pressure range. The third row shows lightning contributions to the free tropospheric NO_2 as taken from the GMI model. Note that we use a log scale for NO_2 VMRs to highlight seasonal and spatial variations. As we sample GMI output over the OMI cloud pressure range, we do not obtain GMI NO_2 VMRs where OMI NO_2 VMRs and the corresponding cloud pressure range are not reported.

In Appendix C, we show additional NO_2 fields for reference including GMI all-sky NO_2 VMR, OMI tropospheric column NO_2 (Bucsela et al., 2013), and GMI tropospheric column NO_2. We note that the magnitudes of NO_2 VMRs from GMI are generally lower than those from OMI NO_2 cloud slicing. Beside the differences magnitudes, the OMI VMR maps show some notable differences with respect to GMI, while the OMI and GMI tropospheric column maps in Appendix C look very similar.

Below, we first describe the features of "cloudy scenes" that distinguish the cloudy scenes from clear conditions and the concurrent possible sampling biases. In the following subsections, we examine the potential contributions from different sources by analyzing temporal/spatial variations of free tropospheric VMRs (Sects. 4.2.2 and 4.2.3) as well as rough vertical profiles (Sect. 4.3).

4.2.1 Potential issues related to satellite sampling in cloudy conditions

Our derived climatology is representative of NO_2 VMRs in highly cloudy conditions with significant cloud pressure variability as explained in Sect. 3.1. Consequently, NO_2 VMRs are not obtained where clouds rarely form (e.g., Sahara) or where cloud pressure variability is small (e.g., oceanic areas with persistent low clouds due to subsidence, such as off the western coasts of South America and southern Africa). Therefore, it is important to interpret our results in the context of the observing conditions. In addition, when comparing cloud-slicing results with those from models, it is important to appropriately sample the model to reflect the observing conditions.

Here, we describe the potential differences between NO_2 VMRs in cloudy and all-sky conditions due to chemistry and transport. One important feature in cloudy conditions is lightning NO_x production; it generally increases NO_2 concentrations as compared with clear-skies. This is especially important in the tropics. In middle to high latitudes, the cloud-slicing NO_2 VMRs are also derived in frontal storms, where uplift of boundary layer pollution and subsequent long-range transport frequently occurs (e.g., in the so-called warm conveyor belt) (Stohl et al., 2003; Zien et al., 2013). This may also increase cloud-slicing NO_2 VMRs as compared with clear-sky conditions. In addition, NO_x chemistry will be different in highly cloudy conditions as compared with clear-skies. For example, NO_2 photolysis rates may be increased above or within bright clouds, but decreased below them.

Comparison of NO_2 VMRs from GMI in cloudy and all-sky conditions may provide an estimate of potential sampling biases. In general, the GMI cloudy NO_2 VMRs are higher than those in all-sky conditions over urban regions (see Fig. C2 in Appendix C for GMI all-sky conditions). Therefore,

in Sect. 4.2, for all comparisons we sample GMI in highly cloudy conditions (cloud optical depth $>$ 10) and consider the potential sampling biases in the interpretation of our derived climatology.

4.2.2 Anthropogenic contributions

In the Northern Hemisphere (NH) winter (December–February), the primary source of free tropospheric NO_2 appears to be anthropogenic emissions; high free tropospheric VMRs are seen over densely populated regions and the lightning contribution is expected to be negligible during these months (top right panel of Fig. 7). Over most of the highly populated areas of North America, southeast (SE) Asia, and Europe, free tropospheric NO_2 VMRs are higher in winter (December–February) as compared with summer (June–August). It is well known that boundary layer NO_2 VMRs are generally higher in winter as compared with summer owing to a longer chemical lifetime in winter; the OMI-derived tropospheric columns (the first row of Fig. C3 in Appendix C), that are dominated by boundary layer pollution in heavily populated areas, also reflect higher values in winter than in summer.

In contrast to NO_2 VMRs from OMI, the NO_2 VMRs from GMI are higher in summer as compared with winter over southeast Asia (the second row of Fig. 7 for cloudy conditions, and Fig. C2 for all-sky conditions), while the tropospheric column NO_2 from GMI is higher in winter in this region (the second row of Fig. C3 in Appendix C). It is well known that boundary layer NO_2 VMRs and thus tropospheric NO_2 columns are higher in winter due to longer lifetimes. Our cloud slicing results show that seasonality of the OMI free tropospheric VMRs is similar to that in the boundary layer VMRs. However, this seasonality is not as apparent in the GMI model. Examination of GMI NO_2 and NO vertical profiles confirms that this is not a simple partitioning problem of NO_x.

Overall, OMI NO_2 VMRs have lower values in the SH during the austral winter as compared with the NH. This is also shown in the GMI output. It should be noted that there are not many large population centers in the SH, particularly at high latitudes, nor as much NO_x contribution from aircraft at high latitudes in the SH as compared with the NH. However, it should also be noted that cloud slicing data are not available around many of the major population centers in the SH (e.g., Johannesburg, South Africa and Sao Paulo, Brazil) owing to a lack of optically thick clouds and/or cloud pressure variation.

Regarding transport of anthropogenic NO_2, we focus on winter months when lightning NO_2 contributions are likely to be small. The OMI cloud slicing NO_2 climatology shows a spatial patterns consistent with pollution outflow from North America and Asia. For example, the persistent Asian northeasterly outflow of NO_2 via the Bering Sea resembles that of CO (e.g., Liang et al., 2004), a tracer of incomplete combustion emissions. The spatial extents of continental outflows are different for the free tropospheric VMRs and tropospheric columns. This might be explained by extended transport at higher altitudes where the NO_2 lifetime is longer.

4.2.3 Lightning contributions

A band of enhanced NO_2 appears extensively during the summer in both hemispheres ($\sim$ 0–30° and possibly higher latitudes in the NH). The low cloud scene pressures (shown in the fifth row of Fig. C1 in Appendix C) in these regions are indicative of frequent convection. In particular, extensive enhancements in summertime NO_2 VMRs over NH tropical and subtropical oceans, are similar to modeled lightning NO_x enhancements in previous studies (e.g., Choi et al., 2008; Allen et al., 2012; Martini et al., 2011; Walker et al., 2010). This suggests that lightning is a major source of free tropospheric NO_2 in tropical and subtropical regions in summer. Because the SH is far less polluted than the NH, potential NO_2 enhancements due to lightning are more apparent there. Finally, we note that these extensive NO_2 enhancements indicated by cloud slicing during summer over oceans are not as apparent in the OMI tropospheric columns.

While the locations of these apparent lightning-enhancements of NO_2 over land are similar in summer in both GMI and OMI data sets, there are a few key differences to note: (1) the seasonality of the NO_2 enhancements over tropical oceans shown in OMI data is not as apparent in the GMI output; in the OMI climatology, the enhancement in oceanic NO_2 VMRs is present in summer, while GMI shows less seasonal variability; (2) There is a stronger land/ocean contrast in GMI lightning-generated NO_2 contribution than is seen in the OMI NO_2 VMR climatology in regions where lightning may be playing a dominant role.

Boersma et al. (2005) have reported similar observations; they inferred a considerable amount of lightning-generated NO_2 over tropical regions using cloudy GOME measurements with similar spatial patterns as shown in our cloud-slicing results. They also compared GOME-derived NO_2 with that from the TM3 chemical transport model. Their study also showed some differences between observations and model simulations in cloudy conditions, presumably related to lightning parameterizations within chemical transport models.

For comparison, we also show maps of free-tropospheric NO_2 climatology obtained with OMCLDO2 cloud data in Fig. D4 of Appendix D2. The OMCLDO2 climatology shows very similar spatial and temporal patterns as compared with that derived using OMCLDRR data presented here with slightly lower VMRs in general. However, the OMCLDO2 climatology does not show a strong signature of lightning-enhanced NO_2 over the tropical North Pacific in June–August as is shown in the OMCLDRR climatology. This is discussed in more detail in Appendix D2.

4.3 Profile analysis

In our above cloud-slicing analysis, we assume that the NO2 VMR profile is uniform within the OMI-observed cloud pressure range for each VMR linear fitting (Sect. 3.1). However, we do not require the VMR profile to be uniform throughout the entire free troposphere. Instead, by collecting VMRs centered at various pressure levels, we are able to infer NO_2 profile information given a large

number of cloudy VMR retrievals. In this section, we highlight tropical portions of the NH and SH to examine potential lightning contributions.

Figure 8 shows variations in the derived NO_2 profiles in tropical regions of the NH and SH. Here, we examine two latitudinal bands with enhanced summertime NO_2 based on the spatial distributions shown in Fig. 7. Again, owing to the large number of samples, the standard errors are relatively small ($\sim 5\,\mathrm{pptv}$). In summer, the NO_2 VMRs increase with altitude in both hemispheres. The profile shapes suggest that NO_2 sources, presumably lightning, are located primarily in the upper troposphere in these regions. This is consistent with aircraft measurements (e.g., Huntrieser et al., 2009) and modeling studies (e.g., Allen et al., 2010, 2012; Martini et al., 2011) of lightning-generated NO_x. In contrast, NO_2 VMR profiles are more uniform in winter, possibly owing to less frequent lightning activity associated with convection in the shifting Inter-Tropical Convergence Zone (ITCZ). We note that the winter baseline NO_2 VMR is higher in NH by approximately a factor of two possibly due to more pollution sources in NH. In contrast, the summertime profiles of NO_2 are very similar in the NH and SH.

Overall, our analysis indicates a capability of the cloud slicing technique to retrieve NO_2 profile information when provided with a relatively large sample size. Our profile results indicate a lightning source in the summer over tropical areas, primarily located in the upper troposphere.

5 Conclusions

We have estimated free tropospheric NO_2 VMRs and stratospheric NO_2 columns using a cloud slicing approach applied to OMI data from 2005 to 2007. Optically thick clouds provide excellent sensitivity of satellite radiances to NO_2 above the cloud scene pressure; they also effectively shield satellite observations from NO_2 below clouds. In order to retrieve NO_2 VMRs, our approach requires a large number of cloudy measurements with substantial cloud pressure variability.

We conducted a detailed comparison between OMI cloud slicing free tropospheric NO_2 VMRs and INTEX-B aircraft in situ measurements. Our analysis shows that the cloud slicing technique provides similar magnitudes as compared with in situ measurements when known satellite biases are taken into consideration. However, individual comparisons of INTEX-B and cloud slicing NO_2 VMRs do not always exhibit good agreement. Small-scale temporal and spatial variability, poor collocation, and fairly large OMI measurement uncertainties contribute to these discrepancies.

We generated global seasonal maps of free tropospheric NO_2 VMRs as well as free tropospheric NO_2 vertical profiles over selected regions. With appropriate data filtering over a three year time period, we obtain a sufficient number of cloudy OMI measurements to cover most of the Earth. Confidence intervals for individual cloud slicing VMRs are fairly large; however, averaging over nine months (3 months $\times$ 3 yr) reduces random errors and provides a reasonable estimate of the mean values. The free-tropospheric NO_2 VMR climatology shows distinct spatial and seasonal patterns;

these patterns differ from those of OMI-estimated tropospheric NO_2 columns. The combination of mapped and profile analyses indicates that spatial patterns of the OMI-derived free tropospheric NO_2 are consistent with (1) uplifted anthropogenic NO_2 over densely populated regions; (2) continental outflow of anthropogenic NO_2; and (3) lightning-generated NO_x, particularly in summer months at low to middle latitudes with a source located primarily in the upper troposphere. Anthropogenic sources appear to dominate in the winter hemisphere, especially in the Northern Hemisphere at high latitudes near heavily populated regions, while lightning contributions dominate over ocean at low to middle latitudes in summer in both hemispheres.

GMI model simulations suggest that NO_2 VMRs vary with cloud conditions by altering the photochemistry. Spatial patterns of continental outflow show general agreement between the OMI cloud slicing climatology and GMI simulations for cloudy conditions. However, some differences, particularly with respect to the seasonality of lightning-generated NO_2 in the tropics and anthropogenic NO_2 in the extra-tropics, are noted.

Our overall analysis shows that the cloud slicing technique can provide valuable information on the free tropospheric distribution of NO_2 that is distinct from the derived tropospheric total columns. In particular, we expect to apply this technique to future geostationary missions including the NASA Earth Ventures Instrument (EVI) 1 selected mission Tropospheric Emissions: Monitoring of Pollution (TEMPO) over North America (Chance et al., 2013) and the Korean Geostationary Environment Monitoring Spectrometer (GEMS) over the Asia–Pacific region (Kim, 2012). These missions should provide excellent cloud slicing results; they will provide improved sampling (with higher spatial and temporal resolutions) as compared with OMI.

Appendix A

Additional details in applying the cloud slicing technique

A1 Data filtering criteria

In order to ensure that appropriate data are used for cloud-slicing, we apply rigorous data filtering criteria. This results in the use of approximately 10–15 % of the available pixel data depending on season and geolocation. The data selection criteria are summarized in Table 1.

We apply the following checks to ensure that only high quality data are used in our analysis. With these checks, approximately 10–15 % of OMI pixels are retained, depending on season and geolocation: (1) we use only pixels with $f_r > 0.9$ to remove OMI pixels with an insufficient cloud shielding of the boundary layer; (2) we remove data with aerosol indices > 1.0, because absorbing aerosols are known to produce biases in the retrieved cloud properties (Vasilkov et al., 2008); (3) we exclude data with solar zenith angles (SZA) $> 80^\circ$; the use of the geometric AMFs may not be appropriate at higher SZAs owing to higher amounts of Rayleigh scattering; (4) we exclude

data affected by snow and ice because UV/VIS cloud measurements cannot differentiate between snow/ice and clouds; In the presence of snow/ice, we cannot be assured of boundary layer cloud shielding. We use a flag for snow- and ice-covered pixels based on the Near-real-time SSM/I EASE-grid daily global Ice and snow concentration and Snow Extent (NISE) data set (Nolin et al., 1998) provided in OMCLDRR product.

We also apply checks to ensure sufficient cloud variability; we only use collections with at least 30 OMI pixels, a cloud pressure standard deviation $> 35\,\mathrm{hPa}$, and a cloud pressure range $> 200\,\mathrm{hPa}$. Finally, we employ outlier checks to remove data that fall outside the range expected from our assumptions including a uniform mixing ratio over the appropriate pressure range and homogeneous stratospheric column over the corresponding area; we empirically selected a threshold of 2σ from an initial linear fit for this check. This outlier check excludes an additional ~3% of the data. With this outlier check, we aim to minimize the effects of in-situ lightning $\mathrm{NO_x}$ production cases in our sampling that may reflect non-uniform mixing ratio profiles that would invalidate our cloud-slicing assumptions.

A2 Application of cloud slicing to seasonal climatology

In order to create a global seasonal climatology of free-tropospheric $\mathrm{NO_2}$ VMRs, we average individual retrievals in three month segments (one for each season) using data collected over 3 yr (2005–2007). We grid the data at a spatial resolution of 6° latitude × 8° longitude.

In Fig. A1, we show two examples of how the $\mathrm{NO_2}$ VMRs are calculated for a single grid box. For these examples, we use only one month in summer (June) and winter (January). The grid box encompasses New York City, NY, USA. In order to remove pixels affected by substantial vertical gradients in the $\mathrm{NO_2}$ VMR, we use only cloudy data with $p_{\mathrm{scene}} <$ a lower boundary (p_{lower}, gray lines) where the mean $\mathrm{NO_2}$ vertical profile is relatively well mixed according GMI; specifically, p_{lower} is pressure above which the absolute magnitude of vertical gradient of monthly-mean $\mathrm{NO_2}$ VMR $< 0.33\,\mathrm{pptv\,hPa^{-1}}$. Note that p_{lower} varies with season (as shown in Fig. A1) and geolocation (not shown). For reference, we also show GMI daily and monthly mean profiles.

Using an OMI pixel collection from a single orbit, we calculate the free tropospheric $\mathrm{NO_2}$ VMR (small black dots), the confidence interval (horizontal bars), and the pressure range (vertical bars). Then, we average the derived single-orbit $\mathrm{NO_2}$ VMRs (weighted inversely by the square of the confidence intervals) to obtain a single representative $\mathrm{NO_2}$ VMR for the given time period (large black dots).

In Fig. A1, we have shown data from one month for simplicity. To construct a seasonal climatology, we use the same spatial grid but a larger temporal window (3 months×3 yr) to reduce the sampling biases and random noise. For quality control of the climatology, we show data only where the $\mathrm{NO_2}$ VMR standard error of the mean $< 50\,\%$ for $\mathrm{NO_2}$ VMR $> 20\,\mathrm{pptv}$ or $\mathrm{NO_2}$ VMR standard error of the mean $< 10\,\mathrm{pptv}$ for $\mathrm{NO_2}$ VMR $\leq 20\,\mathrm{pptv}$. With these criteria, there are some areas

with no OMI-derived NO_2 VMRs. These are mainly areas with little variability in cloud pressure or regions covered with ice/snow.

Appendix B

Additional case studies of OMI and INTEX-B comparisons

We show additional comparisons in which OMI and INTEX-B NO_2 VMR display poor agreement. These discrepancies are presumably caused by small-scale spatial and temporal variations in NO_2 VMRs, different cloud conditions that might alter the NO_x photochemistry, and/or poor collocations.

Figure B1 shows a case with discrepancies likely due to the differences in the locations, times, and the spatial scales of the measurements. The DC-8 profile was taken over a small area near Houston in the morning (~ 8.35 a.m. LT), while the OMI pixel collection covers a large area over Louisiana in the afternoon (~ 1.35 p.m. LT) on the same day; thus the OMI and DC-8 measurements were taken in adjacent locations with a ~ 5 h time gap. The DC-8 NO_2 profile (second column) appears to be affected by local pollution in the 600–800 hPa range. In contrast, OMI retrieves a low NO_2 VMR over a wide area that includes less populated regions. OMI and INTEX-B VMRs show a significant difference of $\sim 57\,\mathrm{pptv}$ in this case.

Figure B2 shows an example of small scale spatial variations in NO_2 profiles as seen by the aircraft measurements. The second column of Fig. B2 shows two DC-8 NO_2 profiles that were taken on the same day at nearby locations. The first column shows the two corresponding OMI pixel collections closest to the DC-8 profiles. In order to differentiate the two cases, the first row uses dark blue for the DC-8 profile and light blue for OMI pixels, and the second row uses red for the DC-8 profile and pink for OMI pixels. Since the two DC-8 profiles encompass many of the same OMI pixels, the shared pixels are marked with purple on the map (top right). Although the two DC-8 profiles are within a close proximity in both time and space, the averaged NO_2 VMRs differ by about $20\,\mathrm{pptv}$, perhaps due to a transported pollution plume. However, since the OMI pixel collections corresponding the two DC-8 profiles share many OMI pixels, this gives similar NO_2 OMI VMRs for the two corresponding DC-8 profiles. As a result, OMI and INTEX-B profiles differ by $\sim 9.5\,\mathrm{pptv}$ in the first row case, while the difference is smaller in the second row case, about $\sim 5\,\mathrm{pptv}$.

Variability of OMI NO_2 VMRs can also cause discrepancies between OMI and INTEX-B VMRs. This variability may be due to actual variability in the NO_2 profile over the course of a day and/or errors in the OMI measurements. Figure B3 shows a case of OMI cloud slicing VMR variation between orbits for one DC-8 NO_2 profile. The first and second panels of Fig. B3 show two OMI pixel collections taken from two adjacent orbits on the same day. They correspond to one DC-8 profile taken over the Pacific north of Hawaii. Even though the OMI pixel collections cover a similar area and time, the resulting NO_2 VMRs differ by $\sim 15\,\mathrm{pptv}$. This variability may be due to a small

scale feature such as a transported pollution plume, altered photochemistry due to the different solar illuminations or cloud conditions, and/or measurement uncertainties in the OMI data, although the differences appear to be outside the expected OMI uncertainties.

Appendix C

Auxiliary data to interpret cloud slicing NO_2 VMR

Here, we show auxiliary data that is helpful for quality assurance and interpretation of the NO_2 VMR climatology. The first row of Fig. C1 shows the gridded numbers of OMI pixel collections that are used to derive the seasonal free tropospheric NO_2 climatology. The maps show a sufficiently large number of collections (> 60) for many areas of interest. Large numbers of collections are available over the frontal storm track regions of the North Atlantic, North Pacific and Southern ocean as well as the intertropical convergence zone (ITCZ). In addition, there are large numbers of orbits at high latitudes ($> 60^\circ$), because these regions can have more than one overpass (orbit) per day. However, some relatively cloud free areas (e.g., the Sahara) as well as oceanic regions, in areas of subsidence with little cloud pressure variability, have smaller numbers of collections (< 20).

The second row of Fig. C1 shows the weighted root mean square (RMS) of 95 % confidence intervals of NO_2 VMRs. As discussed above, the confidence interval is a measure of the fitting uncertainty for single NO_2VMRs derived from individual pixel collections, i.e. a large RMS of the confidence interval means a large uncertainty in the individually fitted NO_2 VMRs. There are two types of regions that have large uncertainties: (1) regions with low numbers of OMI orbits, i.e, small amounts clouds or low cloud pressure variability; (2) areas where NO_2 VMRs are high, e.g., major metropolitan areas. In these regions, we may expect larger variability in the NO_2 VCDs within a single collection.

The third row of Fig. C1 shows maps of standard deviations of the gridded climatological NO_2 VMRs. This is a measure of how much the individually fitted NO_2 VMRs vary in each grid box. Similar to the confidence interval, the standard deviations are large in areas of high NO_2 VMRs (major urban areas and continental plumes) and areas with small clouds amounts and/or small cloud variability (deserts and oceans near 20° N latitude). In addition, high standard deviations are present near $\sim 60^\circ$ S in September–November, possibly owing to stratospheric variability and/or larger errors at high solar zenith angles.

The fourth row of Fig. C1 shows maps of the standard error of the mean for the gridded NO_2 VMR climatology (i.e., the standard deviation divided by square root of the number of measurements). The standard errors provide an estimate of uncertainty for the spatial and temporal variations shown in the climatology (in the absence of a constant bias). We use this quantity for quality control as described in Sect. 4.2.

The fifth row of Fig. C1 shows maps of the OMCLDRR cloud scene pressure for the gridded NO_2 VMR climatology. Owing to significant light penetration inside clouds, the lowest mean cloud pressures are around 450 hPa, well below the typical cloud top pressures. The cloud pressures also vary with season.

Figure C2 shows seasonal mean GMI free tropospheric NO_2 VMRs for all-sky conditions. While the maps of all-sky VMR show similar patterns as compared with those of cloudy conditions, all-sky NO_2 VMRs are generally lower over urban regions and higher over oceans than cloudy NO_2 VMRs.

Figure C3 shows tropospheric column NO_2 from OMI (upper row) and GMI (bottom row). OMI and GMI tropospheric columns NO_2 agree very well, showing higher columns in winter and lower columns in summer over major urban areas. This seasonal variation is also shown in the OMI climatology of free tropospheric NO_2 VMR as presented in Sect. 4.2.2.

Appendix D

Sample results from different data sets

D1 Geometric AMF sample results

Here, we show results obtained using geometric cloudy AMFs with the OMCLDRR cloud OCP values. Similar to Fig. 6, Fig. D1 shows a scattergram of INTEX-B and OMI cloud slicing NO_2 VMRs. The left panel shows all available matchups between INTEX-B and OMI, and the right panel shows matchups where the standard error of the mean of INTEX-B measurements < 5 pptv. The mean difference between INTEX-B and OMI NO_2 VMRs is greater when using geometric AMF as compared with the near-Lambertian AMF. However, the RMS difference between INTEX-B and OMI NO_2 VMRs is smaller with geometric AMFs.

Similar to the first row of Fig. 7, the first row of Fig. D2 shows global maps of the free tropospheric NO_2 climatology obtained with geometric AMFs. The second row of Fig. D4 shows the difference in NO_2 computed using geometric and near-Lambertian AMFs. NO_2 VMRs computed using geometric AMFs show similar spatial patterns and seasonality as compared with that computed using near-Lambertian AMFs; for example, both climatologies show high NO_2 VMRs near major urban areas and the outflow regions and high NO_2 in tropical regions affected by lightning. Overall, NO_2 VMRs from geometric AMFs have higher magnitudes as compared with near-Lambertian AMF results. These VMR differences are highest in high-latitude oceanic areas during summer. This might result from the combination of cloud pressure and a priori NO_2 profile used in near-Lambertian AMF formulation. In these regions, clouds form at very high pressure levels (low altitudes) as shown in the fifth row of Fig. C2, where geometric and near-Lambertian AMFs behave differently as explained in Sect. 3.2. Moreover, there is no ground-based NO_x source, which makes the actual NO_2 profile different from the C-shaped NO_2 profile used in the near-Lambertian AMF calculations.

D2 OMCLDO2 sample results

While we used near-Lambertian cloudy AMFs and OMCLDRR cloud parameters for analysis in the main text, here we show results obtained when using geometric AMFs and cloud parameters from the OMCLDO2 product. We note that these results should be compared with those in Appendix D1, rather than Sect. 4.2. Similar to Fig. 6, Fig. D3 shows a scattergram of INTEX-B and OMI cloud slicing NO_2 VMRs, but using OMCLDO2 cloud data. As above for OMCLDRR, the left panel shows results from all available matchups between INTEX-B and OMI, and the middle panel shows matchups where the standard error of the mean of INTEX-B measurement $< 5\,\mathrm{pptv}$. We note that the number of matchups is different for the OMCLDRR and OMCLDO2 results. Since OMCLDRR and OMCLDO2 report slightly different cloud scene pressures for the same OMI pixel, differences in the cloud data results in different quality control decisions, and this produces the different numbers of successful collocations. Similarly, the reported INTEX-B VMRs used in the scattergram can change with the cloud pressure data set as the INTEX-B VMRs are sampled over the appropriate range of OMI-derived cloud pressures.

The RMS differences between INTEX-B and OMI NO_2 VMRs using both cloud products are similar in magnitude. OMCLDO2 results have a slightly lower correlation with INTEX-B if we exclude INTEX-B measurement with large standard errors ($> 5\,\mathrm{pptv}$).

Similar to the two upper rows of Fig. 7, Fig. D4 shows global maps of the free tropospheric NO_2 climatology obtained with OMCLDO2 cloud parameters. OMCLDO2 NO_2 VMRs (first row) overall have slightly lower magnitudes as compared with OMCLDRR results. The spatial and temporal patterns of OMCLDO2 NO_2 VMR over densely populated regions as well as the continental outflow patterns are similar to those from OMCLDRR. NO_2 VMRs in areas that are thought be affected by lightning, however, display some differences. In OMCLDRR results, lightning-generated NO_2 appears to be present extensively during summer in the both hemispheres. In OMCLDO2 results, we can see an indication of lightning-generated NO_2 in the SH in December–February. While we see possible lightning NO_2 signatures with OMCLDO2 over the Gulf of Mexico, the north equatorial Atlantic, and India, there is not a significant lightning NO_2 feature in the low latitudes of the NH Pacific in June–August as was shown in OMCLDRR results. The reasons for these differences are not well understood. Joiner et al. (2010) showed that there is a high frequency of multi-layer clouds in the NH Pacific. The two cloud algorithms may behave differently in these complex conditions as Raman scattering has a linear response with cloud pressure, while oxygen dimer absorption has a pressure-squared dependence.

Acknowledgements. This material is based upon work supported by the National Aeronautics and Space Administration under agreement NNH10ZDA001N-AURA issued through the Science Mission Directorate for the Aura Science Team managed by Kenneth Jucks. We thank the the OMI data processing team and algorithm developers, particularly F. Boersma and P. Veefkind, the GMI team, (lead by S. Strahan), and R. Cohen for pro-

viding the data used for this study. We also thank E. Celarier, P. K. Bhartia, L. Lamsal, R. Salawitch, T. Canty, and S. Marchenko for helpful discussions. Finally, the authors express special thanks to the two anonymous referees and editor M. Van Roozendael for valuable comments that improved this paper.

References

Acarreta, J. R., De Haan, J. F., and Stammes, P.: Cloud pressure retrieval using the O_2-O_2 absorption band at 477 nm, J. Geophys. Res., 109, D05204, doi:10.1029/2003JD003915, 2004.

Ahmad, Z., Bhartia, P. K., and Krotkov, N.: Spectral properties of backscattered UV radiation in cloudy atmospheres, J. Geophys. Res., 109, 0148–0227, doi:10.1029/2003JD003395, 2004.

Allen, D., Pickering, K., Duncan, B., and Damon, M.: Impact of lightning NO emissions on North American photochemistry as determined using the Global Modeling Initiative (GMI) model, J. Geophys. Res., 115, D22301, doi:10.1029/2010JD014062, 2010.

Allen, D. J., Pickering, K. E., Pinder, R. W., Henderson, B. H., Appel, K. W., and Prados, A.: Impact of lightning-NO on eastern United States photochemistry during the summer of 2006 as determined using the CMAQ model, Atmos. Chem. Phys., 12, 1737–1758, doi:10.5194/acp-12-1737-2012, 2012.

Avery, M., Twohy, C., McCabe, D., Joiner, J., Severance, K., Atlas, E., Blake, D., Bui, T. P., Crounse, J., Dibb, J., Diskin, G., Lawson, P., McGill, M., Rogers, D., Sachse, G., Scheuer, E., Thompson, A. M., Trepte, C., Wennberg, P., and Ziemke, J.: Convective distribution of tropospheric ozone and tracers in the Central American ITCZ region: Evidence from observations during TC4, J. Geophys. Res., 115, D00J21, doi:10.1029/2009JD013450, 2010.

Beirle, S., Platt, U., von Glasow, R., Wenig, M., and Wagner, T.: Estimate of nitrogen oxide emissions from shipping by satellite remote sensing, Geophys. Res. Lett., 31, L18102, doi:10.1029/2004GL020312, 2004.

Beirle, S., Spichtinger, N., Stohl, A., Cummins, K. L., Turner, T., Boccippio, D., Cooper, O. R., Wenig, M., Grzegorski, M., Platt, U., and Wagner, T.: Estimating the NOx produced by lightning from GOME and NLDN data: a case study in the Gulf of Mexico, Atmos. Chem. Phys., 6, 1075–1089, doi:10.5194/acp-6-1075-2006, 2006.

Beirle, S., Salzmann, M., Lawrence, M. G., and Wagner, T.: Sensitivity of satellite observations for freshly produced lightning NO_x, Atmos. Chem. Phys., 9(3), 1077–1094, 2009.

Beirle, S., Boersma, K. F., Platt, U., Lawrence, M. G., and Wagner, T.: Megacity emissions and lifetimes of nitrogen oxides probed from space, Science, 333, 1737–1739, 2011.

Belmonte Rivas, M., Veefkind, P., Boersma, F., Levelt, P., Eskes, H., and Gille, J.: Intercomparison of daytime stratospheric NO_2 satellite retrievals and model simulations, Atmos. Meas. Tech. Discuss., 7, 895–948, doi:10.5194/amtd-7-895-2014, 2014.

Bey, I., Jacob, D. J., Yantosca, R. M., Logan, J. A., Field, B. D., Fiore, A. M., Li, Q., Liu, H., Mickley, L. J., and Schultz, M. G.: Global modeling of tropospheric chemistry with assimilated meteorology: model description and evaluation, J. Geophys. Res., 106, 23073–23095, 2001.

Boersma, K. F., Eskes, H. J., Meijer, E. W., and Kelder, H. M.: Estimates of lightning NO_x production from GOME satellite observations, Atmos. Chem. Phys., 5, 2311–2331, doi:10.5194/acp-5-2311-2005, 2005.

Boersma, K. F., Eskes, H. J., Veefkind, J. P., Brinksma, E. J., van der A, R. J., Sneep, M., van den Oord, G. H. J., Levelt, P. F., Stammes, P., Gleason, J. F., and Bucsela, E. J.: Near-real time retrieval of tropospheric NO_2 from OMI, Atmos. Chem. Phys., 7, 2103–2118, doi:10.5194/acp-7-2103-2007, 2007.

Boersma, K. F., Jacob, D. J., Bucsela, E. J., Perring, A. E., Dirksen, R., van der A, R. J., Yantosca, R. M., Park, R. J., Wenig, M. O., and Bertram, T. H.: Validation of OMI tropospheric NO_2 observations during INTEX-B and application to constrain NO_x emissions over the eastern United States and Mexico, Atmos.

Environ., 42, 4480–4497, doi:10.1016/j.atmosenv.2008.02.004, 2008.

Boersma, K. F., Eskes, H. J., Dirksen, R. J., van der A, R. J., Veefkind, J. P., Stammes, P., Huijnen, V., Kleipool, Q. L., Sneep, M., Claas, J., Leitão, J., Richter, A., Zhou, Y., and Brunner, D.: An improved tropospheric NO_2 column retrieval algorithm for the Ozone Monitoring Instrument, Atmos. Meas. Tech., 4, 1905–1928, doi:10.5194/amt-4-1905-2011, 2011.

Boersma, K. F., van Geffen, J., Maasakkers, J. D., Eskes, H. J., Williams, J. W., and Veefkind, J. P.: Algorithm improvements for (TROP)OMI NO_2 retrievals (towards v3.0), presented at the OMI Science Team Meeting, De Bilt, The Netherlands, 2014.

Bovensmann, H., Burrows, J. P., Buchwitz, M., Frerick, J., Noël, S., Rozanov, V. V., Chance, K. V., and Goede, A. P. H.: SCIAMACHY: mission objectives and measurement modes, J. Atmos. Sci., 56, 127–150, 1999.

Bowman, K. and Henze, D. K.: Attribution of direct ozone radiative forcing to spatially resolved emissions, Geophys. Res. Lett., 39, L22074, doi:10.1029/2012GL053274, 2012.

Brook, J. R., Burnett, R. T., Dann, T. F., Cakmak, S., Goldberg, M. S., Fan, X., and Wheeler, A. J.: Further interpretation of the acute effect of nitrogen dioxide observed in Canadian time series studies, J. Expo. Sci. Env. Epid., 17, S36–S44, 2007.

Bucsela, E. J., Celarier, E. A., Wenig, M. O., Gleason, J. F., Veefkind, J. P., Boersma, K. F., and Brinksma, E. J.: Algorithm for NO_2 vertical column retrieval from the ozone monitoring instrument, IEEE T. Geosci. Remote, 44, 1245–1258, doi:10.1109/TGRS.2005.863715, 2006.

Bucsela, E. J., Perring, A. E., Cohen, R. C., Boersma, K. F., Celarier, E. A., Gleason, J. F., Wenig, M. O., Bertram, T. H., Wooldridge, P. J., Dirksen, R., and Veefkind, J. P.: Comparison of tropospheric NO_2 from in situ aircraft measurements with near-real-time and standard product data from OMI, J. Geophys. Res., 113, D16S31, doi:10.1029/2007JD008838, 2008.

Bucsela, E. J., Krotkov, N. A., Celarier, E. A., Lamsal, L. N., Swartz, W. H., Bhartia, P. K., Boersma, K. F., Veefkind, J. P., Gleason, J. F., and Pickering, K. E.: A new stratospheric and tropospheric NO_2 retrieval algorithm for nadir-viewing satellite instruments: applications to OMI, Atmos. Meas. Tech., 6, 2607–2626, doi:10.5194/amt-6-2607-2013, 2013.

Castellanos, P. and Boersma, K. F.: Reductions in nitrogen oxides over Europe driven by environmental policy and economic recession, Sci. Rep., 2, 265, doi:10.1038/srep00265, 2012.

Celarier, E. A., Brinksma, E. J., Gleason, J. F., Veefkind, J. P., Cede, A., Herman, J. R., Ionov, D., Goutail, F., Pommereau, J.-P., Lambert, J.-C., van Roozendael, M., Pinardi, G., Wittrock, F., Schönhardt, A., Richter, A., Ibrahim, O. W., Wagner, T., Bojkov, B., Mount, G., Spinei, E., Chen, C. M., Pongetti, T. J., Sander, S. P., Bucsela, E. J., Wenig, M. O., Swart, D. P. J., Volten, H., Kroon, M., and Levelt, P. F.: Validation of Ozone Monitoring Instrument nitrogen dioxide columns, J. Geophys. Res., 113, D15S15, doi:10.1029/2007JD008908, 2008.

Chance, K., Liu, X., Suleiman, R. M., Flittner, D. E., Al-Saadi, J., and Janz, S. J.: Tropospheric Emissions: Monitoring of Pollution (TEMPO), Proc. SPIE, vol. 8866, Earth Observing Systems XVIII, Paper 88660D, San Diego, California, USA, 23 September 2013, doi:10.1117/12.2024479, 2013.

Choi, Y., Wang, Y., Zeng, T., Martin, R. V., Kurosu, T. P., and Chance, K.: Evidence of lightning NO_x and convective transport of pollutants in satellite observations over North America, Geophys. Res. Lett., 32,

L02805, doi:10.1029/2004GL021436, 2005.

Choi, Y., Wang, Y., Zeng, T., Cunnold, D., Yang, E.-S., Martin, R., Chance, K., Thouret, V., and Edgerton, E.: Springtime transitions of NO_2, CO, and O_3 over North America: model evaluation and analysis, J. Geophys. Res., 113, D20311, doi:10.1029/2007JD009632, 2008.

CloudSat Project: Level 2 cloud optical depth product process description and interface control document, version 5.0, available at: http://www.cloudsat.cira.colostate.edu/ICD/2B-TAU/ 2B-TAU PDICD 5.0.pdf, last access: 4 October 2011, Colorado State University, Fort Collins, CO, USA, 2008.

Deirmendjian, D.: Scattering and polarization properties of water clouds and hazes in the visible and infrared, Appl. Opt., 3, 187–196, 1964.

Deirmendjian, D.: Electromagnetic scattering on spherical polydispersions, Elsevier Sci., New York, 290 pp., 1969.

Douglass, A. R., Stolarski, R. S., Strahan, S. E., and Connell, P. S.: Radicals and reservoirs in the GMI chemistry and transport model: comparison to measurements, J. Geophys. Res., 109, D16302, doi:10.1029/2004JD004632, 2004.

Duncan, B. N., Strahan, S. E., Yoshida, Y., Steenrod, S. D., and Livesey, N.: Model study of the cross-tropopause transport of biomass burning pollution, Atmos. Chem. Phys., 7, 3713–3736, doi:10.5194/acp-7-3713-2007, 2007.

Duncan, B. N., Yoshida, Y., de Foy, B., Lamsal, L. N., Streets, D. G., Lu, Z., Pickering, K. E., and Krotkov, N. A.: The observed response of Ozone Monitoring Instrument (OMI) NO_2 columns to NO_x emission controls on power plants in the United States: 2005–2011, Atmos. Environ., 81, 102–111, doi:10.1016/j.atmosenv.2013.08.068, 2013.

Eskes, H. J. and Boersma, K. F.: Averaging kernels for DOAS totalcolumn satellite retrievals, Atmos. Chem. Phys., 3, 1285–1291, 2003.

Frost, G. J., McKeen, S. A., Trainer, M., Ryerson, T. B., Neuman, J. A., Roberts, J. M., Swanson, A., Holloway, J. S., Sueper, D. T., Fortin, T., Parrish, D. D., Fehsenfeld, F. C., Flocke, F., Peckham, S. E., Grell, G. A., Kowal, D., Cartwright, J., Auerbach, N., and Habermann, T.: Effecs of changing power plant NO_x emissions on ozone in the eastern United States: proof of concept, J. Geophys. Res., 111, D12306, doi:10.1029/2005JD006354, 2006.

Fuglestvedt, J., Berntsen, T., Myhre, G., Rypdal, K., and Skeie, R. B.: Climate forcing from the transport sectors, P. Natl. Acad. Sci. USA, 105, 454–458, 2008.

Hains, J. C., Boersma, K. F., Kroon, M., Dirksen, R. J., Cohen, R. C., Perring, A. E., Bucsela, E., Volten, H., Swart, D. P. J., Richter, A., Wittrock, F., Schoenhardt, A., Wagner, T., Ibrahim, O. W., van Roozendael, M., Pinardi, G., Gleason, J. F., Veefkind, J. P., and Levelt, P.: Testing and improving OMI DOMINO tropospheric NO_2 using observations from the DANDELIONS and INTEX-B validation campaigns, J. Geophys. Res., 115, D05301, doi:10.1029/2009JD012399, 2010.

Herman, J., Cede, A., Spinei, E., Mount, G., Tzortziou, M., and Abuhassan, N.: NO_2 column amounts from ground-based Pandora and MFDOAS spectrometers using the direct-sun DOAS technique: intercomparisons and application to OMI validation, J. Geophys. Res., 114, D13307, doi:10.1029/2009JD011848, 2009.

Hild, L., Richter, A., Rozanov, V., and Burrows, J. P.: Air Mass Calculations for GOME Measurements of lightning-produced NO_2, Adv. Space Res., 29(11), 1685–1690, 2002.

Huntrieser, H., Schlager, H., Lichtenstern, M., Roiger, A., Stock, P., Minikin, A., Höller, H., Schmidt, K., Betz, H.-D., Allen, G., Viciani, S., Ulanovsky, A., Ravegnani, F., and Brunner, D.: NO_x production by lightning in Hector: first airborne measurements during SCOUT-O3/ACTIVE, Atmos. Chem. Phys., 9, 8377–8412, doi:10.5194/acp-9-8377-2009, 2009.

Jaeglé, L., Steinberger, L., Martin, R. V., and Chance, K.: Global partitioning of NO_x sources using satellite observations: relative roles of fossil fuel combustion, biomass burning and soil emissions, Faraday Discuss., 130, 407–423, doi:10.1039/b502128f, 2005.

Joiner, J. and Vasilkov, A. P.: First results from the OMI rotational raman scattering cloud pressure algorithm, IEEE T. Geosci. Remote, 44, 1272–1282, 2006.

Joiner, J., Schoeberl, M. R., Vasilkov, A. P., Oreopoulos, L., Platnick, S., Livesey, N. J., and Levelt, P. F.: Accurate satellite-derived estimates of the tropospheric ozone impact on the global radiation budget, Atmos. Chem. Phys., 9, 4447–4465, doi:10.5194/acp-9-4447-2009, 2009.

Joiner, J., Vasilkov, A. P., Bhartia, P. K., Wind, G., Platnick, S., and Menzel, W. P.: Detection of multi-layer and vertically-extended clouds using A-train sensors, Atmos. Meas. Tech., 3, 233–247, doi:10.5194/amt-3-233-2010, 2010.

Joiner, J., Vasilkov, A. P., Gupta, P., Bhartia, P. K., Veefkind, P., Sneep, M., de Haan, J., Polonsky, I., and Spurr, R.: Fast simulators for satellite cloud optical centroid pressure retrievals; evaluation of OMI cloud retrievals, Atmos. Meas. Tech., 5, 529–545, doi:10.5194/amt-5-529-2012, 2012.

Kim, J.: GEMS (Geostationary Environment Monitoring Spectrometer) onboard the GeoKOMPSAT to monitor air quality in high temporal and spatial resolution over Asia–Pacific Region, in: EGU General Assembly 2012, Vienna, Austria, 22–27 April 2012, p. 4051, 2012.

Koelemeijer, R. B. A. and Stammes, P.: Effects of clouds on ozone column retrieval from GOME UV measurements, J. Geophys. Res., 104, 8281–8294, doi:10.1029/1999JD900012, 1999.

Krotkov, N. A., Bucsela, E., Celarier, E., Lamsal, L., Swartz, W., Pickering, K., Duncan, B. N., Janz, S., Herman, J., Yoshida, Y., Yurganov, L., Spinei, E., and Gleason, J.: Improved OMI NO_2 standard product: algorithm, evaluation, and results, the Aura Science Team Meeting, Pasadena, CA, USA, http://aura.gsfc.nasa.gov/project/documents/AuraSTM_Oct2012_OralAbstracts.pdf, 2012.

Lamsal, L. N., Martin, R. V., van Donkelaar, A., Celarier, E. A., Bucsela, E. J., Boersma, K. F., Dirksen, R., Luo, C., and Wang, Y.: Indirect validation of tropospheric nitrogen dioxide 30 retrieved from the OMI satellite instrument: insight into the seasonal variation of nitrogen oxides at northern midlatitudes, J. Geophys. Res., 115, D05302, doi:10.1029/2009JD013351, 2010.

Lamsal, L. N., Martin, R. V., Parrish, D. D., Krotkov. N. A.: Scaling relationship for NO_2 pollution and urban population size: a satellite perspective, Environ. Sci. Technol., 47, 7855, doi:10.1021/es400744g, 2013.

Levelt, P. F., van den Oord, G. H. J., Dobber, M. R., Mälkki, A., Visser, H., de Vries, J., Stammes, P., Lundell, J., and Saari, H.: The Ozone Monitoring Instrument, IEEE T. Geosci. Remote, 44, 1093–1101, doi:10.1109/TGRS.2006.872333, 2006.

Li, Q., Jacob. D. J., Park, R., Wang, Y., Heald, C. L., Hudman, R., and Yantosca, R. M.: North American pollution outflow and the trapping of convectively lifted pollution by upper-level anticyclone, J. Geophys. Res., 110, D10301, doi:10.1029/2004JD005039, 2005.

Liang, Q., Jaeglé, L., Jaffe, D. A., Weiss-Penzias, P., Heckman, A., and Snow, J. A.: Long-range transport of

Asian pollution to the Northeast Pacific: seasonal variations and transport pathways of carbon monoxide, J. Geophys. Res., 109, D23S07, doi:10.1029/2003JD004402, 2004.

Lin, J.-T., McElroy, M. B., and Boersma, K. F.: Constraint of anthropogenic NO_x emissions in China from different sectors: a new methodology using multiple satellite retrievals, Atmos. Chem. Phys., 10, 63–78, doi:10.5194/acp-10-63-2010, 2010.

Martin, R. V., Jacob, D. J., Chance, K., Kurosu, T. P., Palmer, P. I., and Evans, M. J.: Global inventory of nitrogen oxide emissions constrained by space-based observations of NO_2 columns, J. Geophys. Res., 108, 4537, doi:10.1029/2003JD003453, 2003.

Martin, R. V., Sioris, C. E., Chance, K. V., Ryerson, T. B., Bertram, T. H.,Woolridge, P. J., Cohen, R. C., Neuman, J. A., Swanson, A., and Flocke, F. M.: Evaluation of space-based constraints on nitrogen oxide emissions with regional aircraft measurements over and downwind of eastern North America, J. Geophys. Res., 111, D15308, doi:10.1029/2005JD006680, 2006.

Martini, M., Allen, D. J., Pickering, K. E., Stenchikov, G. L., Richter, A., Hyer, E. J., and Loughner, C. P.: The impact of North American anthropogenic emissions and lightning on long-range transport of trace gases and their export from the continent during summers 2002 and 2004, J. Geophys. Res., 116, D07305, doi:10.1029/2010JD014305, 2011.

Munro, R., Eisinger, M., Anderson, C., Callies, J., Corpaccioli, E., Lang, R., Lefebvre, A., Livschitz, Y., and Albinana, A. P.: GOME-2 on MetOp, in: Proc. of the 2006 EUMETSAT Meteorological Satellite Conference, Helsinki, Finland, 12–16 June 2006, EUMETSAT, 48, 2006.

Nolin, A., Armstrong, R. L., and Maslanik, J.: Near Real-Time SSM/I EASE-Grid Daily Global Ice Concentration and Snow Extent, January to March 2004 (updated daily), Digital media, National Snow and Ice Data Center, Boulder, CO, USA, 1998.

Parrish, D. D.: Intercontinental Transport and Chemical Transformation 2002 (ITCT 2K2) and Pacific Exploration of Asian Continental Emission (PEACE) experiments: an overview of the 2002 winter and spring intensives, J. Geophys. Res., 109, D23S01, doi:10.1029/2004JD004980, 2004.

Perring, A. E., Bertram, T. H., Farmer, D. K., Wooldridge, P. J., Dibb, J., Blake, N. J., Blake, D. R., Singh, H. B., Fuelberg, H., Diskin, G., Sachse, G., and Cohen, R. C.: The production and persistence of $\Sigma RONO_2$ in the Mexico City plume, Atmos. Chem. Phys., 10, 7215–7229, doi:10.5194/acp-10-7215-2010, 2010.

Pickering, K. E., Wang, Y., Tao, W.-K., Price, C., and Müller, J.-F.: Vertical distributions of lightning NO_x for use in regional and global chemical transport models, J. Geophys. Res., 103, 31203–31216, doi:10.1029/98JD02651, 1998.

Price, C. and Rind, D.: A simple lightning parameterization for calculating global lightning distributions, J. Geophys. Res., 97, 9919–9933, 1992.

Price, C., Penner, J., and Prather, M.: NO_x from lightning, Part I: Global distribution based on lightning physics, J. Geophys. Res., 102, 5929–5941, 1997.

Reidmiller, D. R., Jaffe, D. A., Chand, D., Strode, S., Swartzendruber, P., Wolfe, G. M., and Thornton, J. A.: Interannual variability of long-range transport as seen at the Mt. Bachelor observatory, Atmos. Chem. Phys., 9, 557–572, doi:10.5194/acp-9-557-2009, 2009.

Richter, A. and Burrows, J. P.: Retrieval of tropospheric NO_2 from GOME measurements, Adv. Space Res., 29, 1673–1683, 2002.

Richter, A., Burrows, J. P., Nüß, H., Granier, C., and Niemeier, U.: Increase in tropospheric nitrogen dioxide over China observed from space, Nature, 437, 129–132, doi:10.1038/nature04092, 2005.

Rienecker, M. M., Suarez, M. J., Gelaro, R., Todling, R., Bacmeister, J., Liu, E., Bosilovich, M. G., Schubert, S. D., Takacs, L., Kim, G.-K., Bloom, S., Chen, J., Collins, D., Conaty, A., da Silva, A., Gu, W., Joiner, J., Koster, R. D., Lucchesi, R., Molod, A., Owens, T., Pawson, S., Pegion, P., Redder, C. R., Reichle, R., Robertson, F. R., Ruddick, A. G., Sienkiewicz, M., and Woollen, J.: MERRA: NASA's Modern-Era Retrospective Analysis for Research and Applications, J. Climate, 24, 3624–3648, doi:10.1175/JCLI-D-11-00015.1, 2011.

Russell, A. R., Valin, L. C., Bucsela, E. J., Wenig, M. O., and Cohen, R. C.: Space-based constraints on spatial and temporal patterns of NO_x emissions in California, 2005–2008, Environ. Sci. Technol., 44, 3608–3615, doi:10.1021/es903451j, 2010.

Russell, A. R., Valin, L. C., and Cohen, R. C.: Trends in OMI NO_2 observations over the United States: effects of emission control technology and the economic recession, Atmos. Chem. Phys., 12, 12197–12209, doi:10.5194/acp-12-12197-2012, 2012.

Shindell, D. and Faluvegi, G.: Climate response to regional radiative forcing during the twentieth century, Nat. Geosci., 2, 294–300, doi:10.1038/ngeo473, 2009.

Singh, H. B., Brune, W. H., Crawford, J. H., Flocke, F., and Jacob, D. J.: Chemistry and transport of pollution over the Gulf of Mexico and the Pacific: spring 2006 INTEX-B campaign overview and first results, Atmos. Chem. Phys., 9, 2301–2318, doi:10.5194/acp-9-2301-2009, 2009.

Sneep, M., de Haan, J. F., Stammes, P., Wang, P., Vanbauce, C., Joiner, J., Vasilkov, A. P., and Levelt, P. F.: Three-way comparison between OMI and PARASOL cloud pressure products, J. Geophys. Res., 113, D15S23, doi:10.1029/2007JD008694, 2008.

Solomon, S., Portmann, R. W., Sanders, R. W., and Daniels, J. S.: On the role of nitrogen dioxide in the absorption of solar radiation, J. Geophys. Res., 104, 12047–12058, 1999.

Spurr, R. J. D., Kurosu, T. P., and Chance, K.: A linearized discrete ordinate radiative transfer model for atmospheric remote sensing retrieval, J. Quant. Spectrosc. Ra., 68, 689–735, 2001

Stammes, P., Sneep, M., de Haan, J. F., Veefkind, J. P., Wang, P., and Levelt, P. F.: Effective cloud fractions from the Ozone Monitoring Instrument: theoretical framework and validation, J. Geophys. Res., 113, D16S38, doi:10.1029/2007JD008820, 2008.

Stohl, A., Huntrieser, H., Richter, A., Beirle, S., Cooper, O., Eckhardt, S., Forster, C., James, P., Spichtinger, N., Wenig, M., Wagner, T., Burrows, J. P., and Platt, U.: Rapid intercontinental air pollution transport associated with a meteorological bomb, Atmos. Chem. Phys., 3, 969–985, 2003

Strahan, S. E., Duncan, B. N., and Hoor, P.: Observationally derived transport diagnostics for the lowermost stratosphere and their application to the GMI chemistry and transport model, Atmos. Chem. Phys., 7, 2435–2445, doi:10.5194/acp-7-2435-2007, 2007.

Thornton, J. A., Wooldridge, P. J., and Cohen, R. C.: Atmospheric NO_2: in situ laser-induced fluorescence detection at parts per trillion mixing ratios, Anal. Chem., 72, 528–539, 2000.

Vasilkov, A., Joiner, J., Spurr, R., Bhartia, P. K., Levelt, P., and Stephens, G.: Evaluation of the OMI cloud pressures derived from rotational Raman scattering by comparisons with other satellite data and radiative transfer simulations, J. Geophys. Res., 113, D15S19, doi:10.1029/2007JD008689, 2008.

Vasilkov, A. P., Joiner, J., Oreopoulos, L., Gleason, J. F., Veefkind, P., Bucsela, E., Celarier, E. A., Spurr, R. J. D., and Platnick, S.: Impact of tropospheric nitrogen dioxide on the regional radiation budget, Atmos. Chem. Phys., 9, 6389–6400, doi:10.5194/acp-9-6389-2009, 2009.

Walker, T. W., Martin, R. V., van Donkelaar, A., Leaitch, W. R., MacDonald, A. M., Anlauf, K. G., Cohen, R. C., Bertram, T. H., Huey, L. G., Avery, M. A., Weinheimer, A. J., Flocke, F. M., Tarasick, D. W., Thompson, A. M., Streets, D. G., and Liu, X.: Trans-Pacific transport of reactive nitrogen and ozone to Canada during spring, Atmos. Chem. Phys., 10, 8353–8372, doi:10.5194/acp-10-8353-2010, 2010.

Wang, Y., Choi, Y., Zeng, T., Ridley, B., Blake, N., Blake, D., and Flocke, F.: Late-spring increase of trans-Pacific pollution transport in the upper troposphere, Geophys. Res. Lett., 33, L01811, doi:10.1029/2005GL024975, 2006.

Wild, O., Prather, M. J., and Akimoto, H.: Indirect long-term global radiative cooling from NO_x emissions, Geophys. Res. Lett., 28, 1719–1722, 2001.

Witte, J. C., Schoeberl, M. R., Douglass, A. R., Gleason, J. F., Krotkov, N. A., Gille, J. C., Pickering, K. E., and Livesey, N.: Satellite observations of changes in air quality during the 2008 Beijing Olympics and Paralympics, Geophys. Res. Lett., 36, L17803, doi:10.1029/2009GL039236, 2009.

Zhang, L., Jacob, D. J., Boersma, K. F., Jaffe, D. A., Olson, J. R., Bowman, K. W., Worden, J. R., Thompson, A. M., Avery, M. A., Cohen, R. C., Dibb, J. E., Flock, F. M., Fuelberg, H. E., Huey, L. G., McMillan, W. W., Singh, H. B., and Weinheimer, A. J.: Transpacific transport of ozone pollution and the effect of recent Asian emission increases on air quality in North America: an integrated analysis using satellite, aircraft, ozonesonde, and surface observations, Atmos. Chem. Phys., 8, 6117–6136, doi:10.5194/acp-8-6117-2008, 2008.

Ziemke, J. R., Chandra, S., and Bhartia, P. K.: "Cloud slicing": a new technique to derive upper tropospheric ozone from satellite measurements, J. Geophys. Res., 106, 9853–9867, 2001.

Ziemke, J. R., Chandra, S., and Bhartia, P. K.: Upper tropospheric ozone derived from the cloud slicing technique: implications for large-scale convection, J. Geophys. Res., 108, 4390, doi:10.1029/2002JD002919, 2003.

Ziemke, J. R., Chandra, S., and Bhartia, P. K.: A 25 yr data record of atmospheric ozone in the Pacific from Total Ozone Mapping Spectrometer (TOMS) cloud slicing: implications for ozone trends in the stratosphere and troposphere, J. Geophys. Res., 110, D15105, doi:10.1029/2004JD005687, 2005.

Ziemke, J. R., Joiner, J., Chandra, S., Bhartia, P. K., Vasilkov, A., Haffner, D. P., Yang, K., Schoeberl, M. R., Froidevaux, L., and Levelt, P. F.: Ozone mixing ratios inside tropical deep convective clouds from OMI satellite measurements, Atmos. Chem. Phys., 9, 573–583, doi:10.5194/acp-9-573-2009, 2009.

Zien, A. W., Richter, A., Hilboll, A., Blechschmidt, A.-M., and Burrows, J. P.: Systematic analysis of tropospheric NO_2long-range transport events detected in GOME-2 satellite data, Atmos. Chem. Phys. Discuss., 13, 30945–31012, doi:10.5194/acpd-13-30945-2013, 2013

Zhang, Q., Streets, D. G., He, K.,Wang, Y., Richter, A., Burrows, J. P., Uno, I., Jang, C. J., Chen, D., Yao, Z., and Lei, Y.: NO_x emission trends for China, 1995–2004: the view from the ground 15 and the view from space, J. Geophys. Res., 112, D22306, doi:10.1029/2007jd008684, 2007.

Table 1. OMI data filtering criteria for cloud slicing approach.

Individual pixel	Cloud radiance fraction (f_r)	> 0.9
	UV aerosol index	< 1.0
	Solar zenith angle (SZA)	$< 80°$
	Snow and ice flag	$= 0$ (not affected by snow/ice)
Pixel collection	Number of OMI Pixels	> 30
	Range of cloud effective scene pressure (p_{scene})	$> 200\,\text{hPa}$
	Standard deviation of cloud effective scene pressure (p_{scene})	$> 35\,\text{hPa}$
	Gradient of NO_2 VMR over pressure ($\text{dVMR}/\text{d}p$)*	$< 0.33\,\text{pptv}\,\text{hPa}^{-1}$

* Obtained from INTEX-B or GMI profiles.

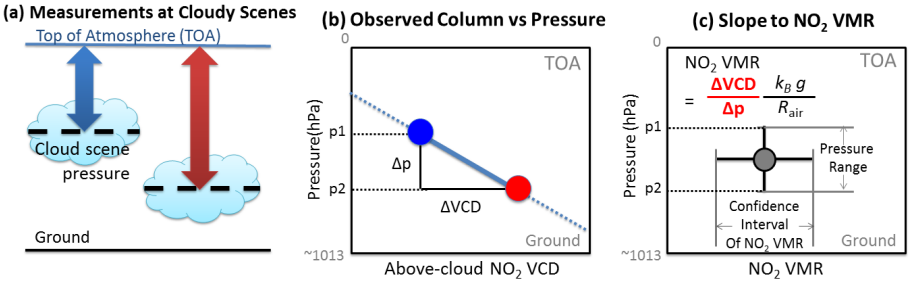

Fig. 1. Schematic view of the cloud slicing technique (not to scale): **(a)** two above-cloud NO_2 column measurements at different cloud scene pressures (blue: column with lower scene pressure; and red: column with higher scene pressure); **(b)** the measurements shown on a pressure-column coordinate plane; **(c)** NO_2 VMR derived from the slope of above-cloud NO_2 VCD versus cloud scene pressure with confidence interval (horizontal error bar) and pressure range (vertical error bar); **(d)** stratospheric column NO_2 derived by extrapolating the linear fit to the tropopause.

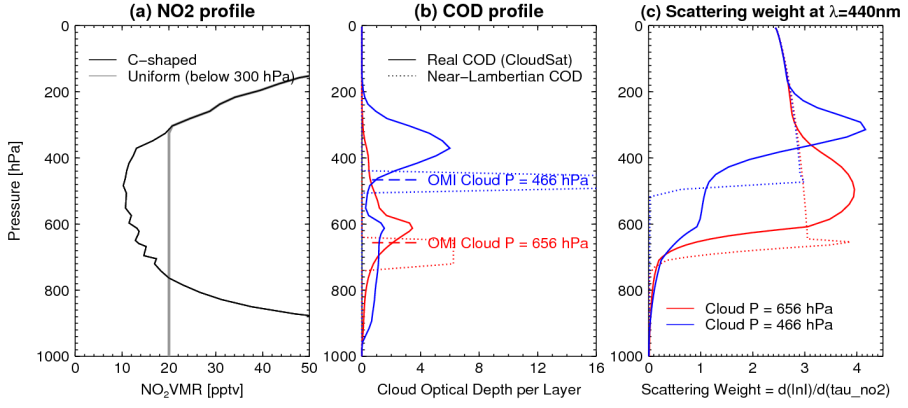

Fig. 2. Experimental settings to simulate OMI above-cloud NO_2 VCD observations: (a) NO_2 profiles used in the AMF calculations, (b) cloud optical depth (COD) profiles used in the radiative transfer calculations, and (c) scattering weight profiles from the radiative transfer calculations corresponding to COD profiles in (b). See text for more details.

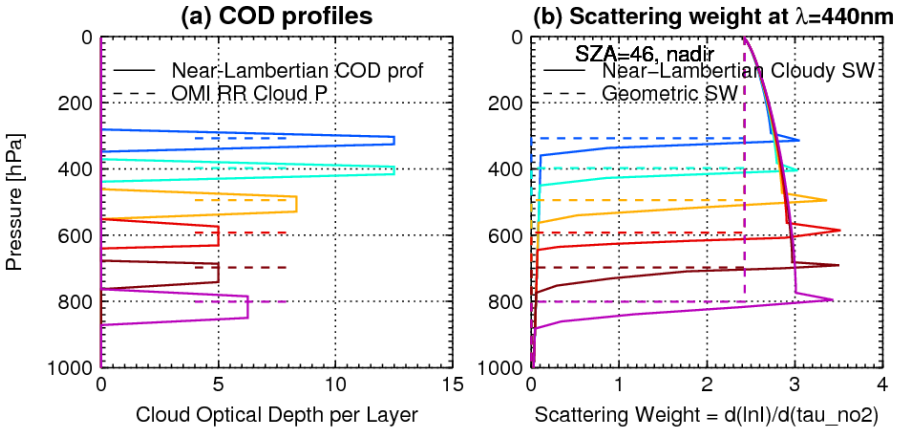

Fig. 3. (a) Near-Lambertian COD profiles (solid lines) that correspond to various cloud OCPs (dashed lines), (b) scattering weights calculated using near-Lambertian COD profiles (solid lines) accompanied by geometric weighting functions (dashed lines).

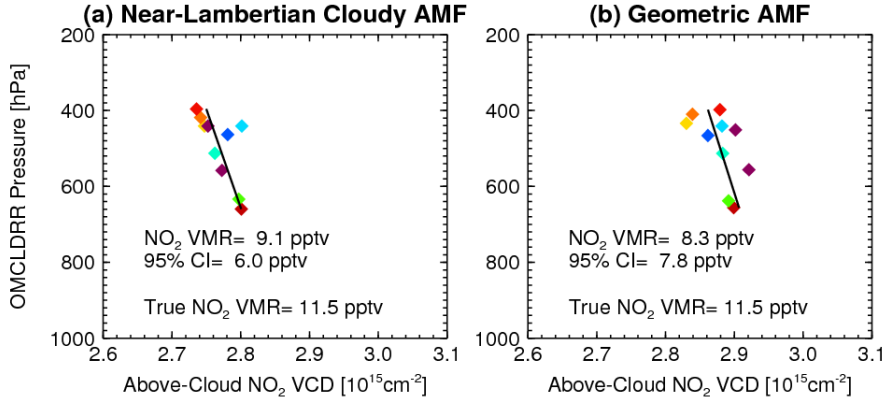

Fig. 4. NO_2 VMRs derived from simulated OMI cloud OCPs and above-cloud NO_2 VCDs using (a) geometric AMFs, and (b) near-Lambertian cloudy AMFs.

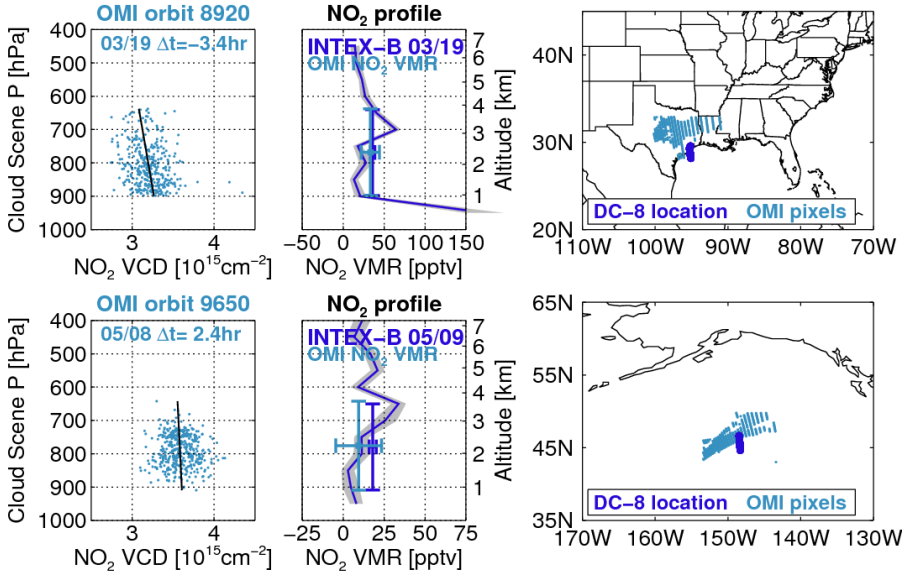

Fig. 5. Examples of relatively good agreement between OMI cloud slicing VMRs and INTEX-B NO_2 profiles near Houston, Texas, US (top row) and the northeastern Pacific (bottom row). In each example, left: OMI above-cloud NO_2 column versus cloud scene pressure (similar to Fig. 1b); center: INTEX-B NO_2 profiles (dark blue line), INTEX-B NO_2 VMR averaged over the OMI pressure range (dark blue square with error bars), and OMI-derived NO_2 VMR (light blue square with error bars); right: locations of OMI and INTEX-B aircraft measurements.

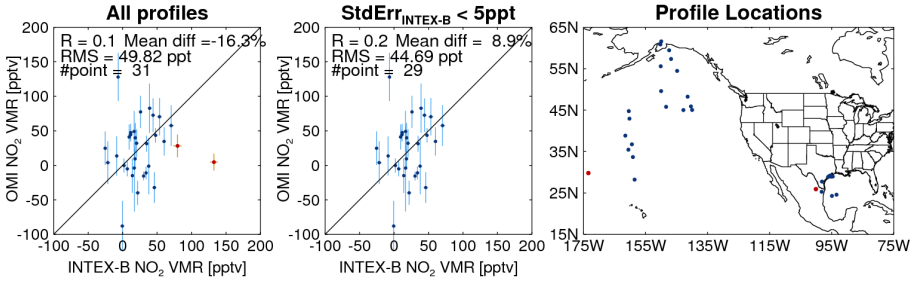

Fig. 6. Scattergram of INTEX-B and OMI cloud slicing NO_2 VMRs; left: all available collocations of INTEX-B and OMI NO_2 VMR; middle: collocations where the INTEX-B standard error of the mean $< 5\,\mathrm{pptv}$; right: locations of the profiles. Red shows cases where the INTEX-B standard error of the mean $> 5\,\mathrm{pptv}$.

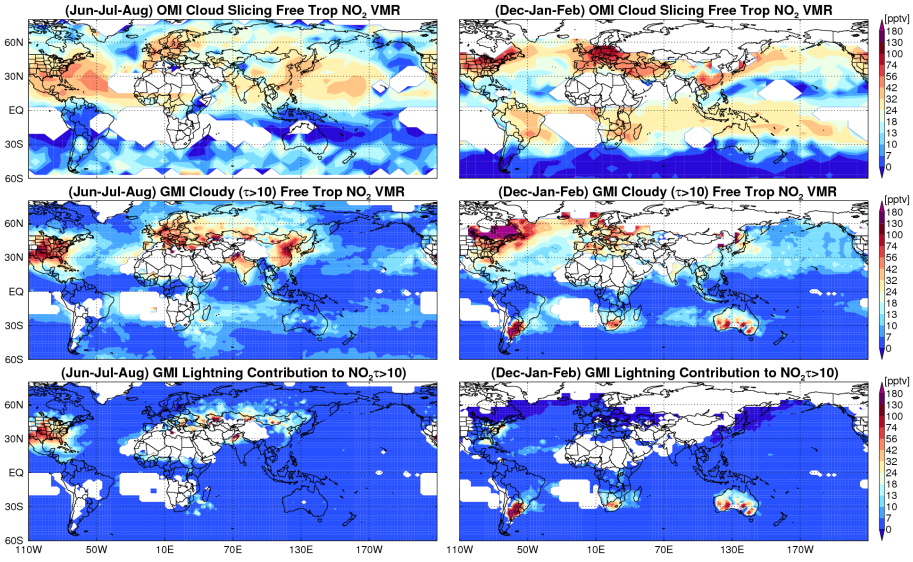

Fig. 7. For June–August (left column) and December–February (right column) averages over 2005–2007; first row: climatology of free tropospheric NO_2 VMR; second row: cloudy ($\tau > 10$) GMI free tropospheric NO_2 VMR; third row: GMI lightning contribution to the free tropospheric NO_2 VMRs.

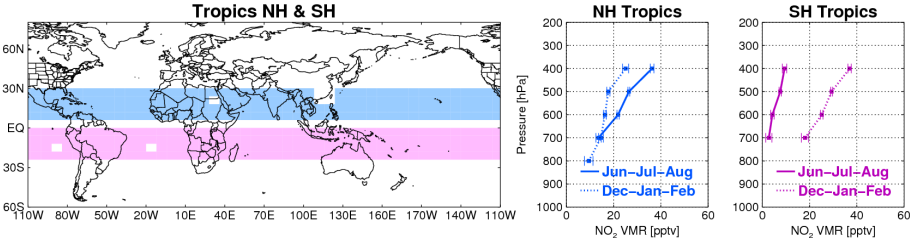

Fig. 8. Left: sampling areas for profiles over tropics of NH (blue) and SH (purple); center: NO_2 profiles over NH tropics for June–August (blue solid line) and December–February (blue dotted line) with standard errors; right: NO_2 profiles over SH tropics for June–August (purple solid line) and December–February (purple dotted line) for 2005–2007.

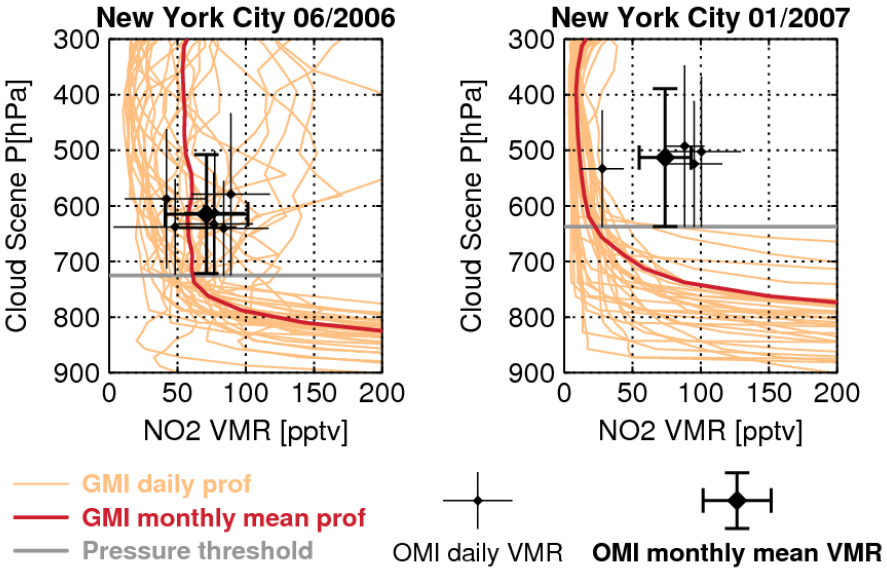

Fig. A1. Example of calculating a climatological free tropospheric NO_2 VMR for a grid box that encompasses New York City; left: May 2005; right: January 2007; lines show daily (orange) and monthly mean (red) GMI NO_2 profiles. Grey horizontal lines show the pressure threshold above which the NO_2 vertical gradient is $< 0.33\,\mathrm{pptv\,hPa^{-1}}$. Not the actual data used in the main text.

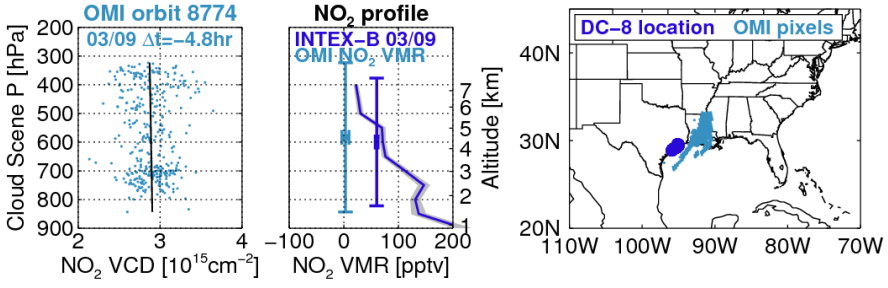

Fig. B1. Similar to Fig. 5, but showing a case with a discrepancy between satellite and aircraft measurements, possibly due to poor collocation, with INTEX-B measurements near Houston, Texas, US and OMI measurements over Louisiana, US.

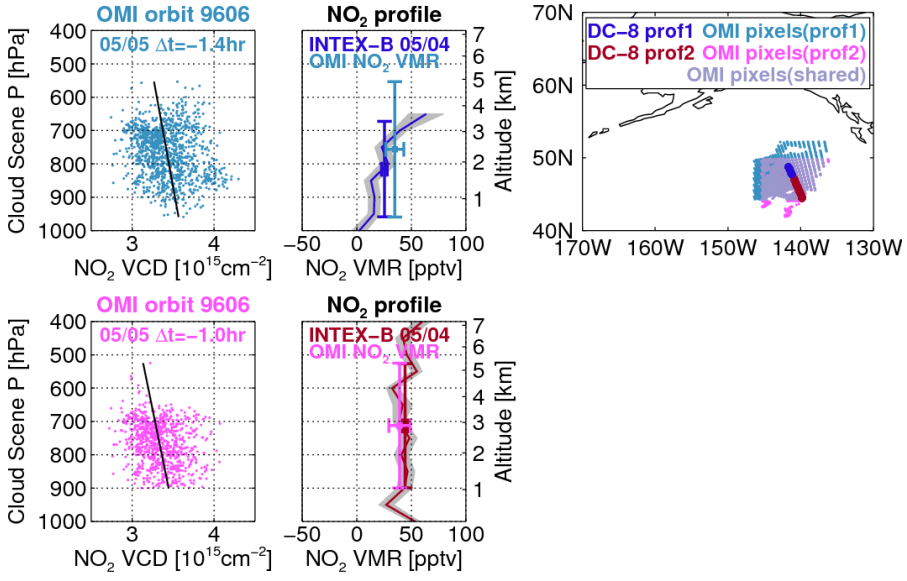

Fig. B2. Similar to Fig. B1, showing another example over the northeastern Pacific with a discrepancy between satellite and aircraft data apparently due to small-scale spatial variations in the INTEX-B NO_2 profiles.

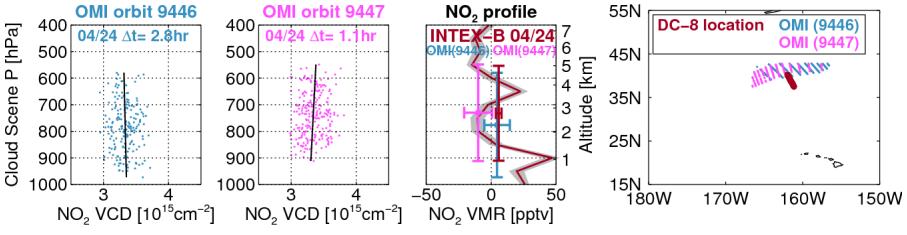

Fig. B3. Similar to Fig. 5, but showing an example of variation in OMI NO_2 VMRs over two adjacent orbits (1.5 h time difference) at the same location north of Hawaii, US.

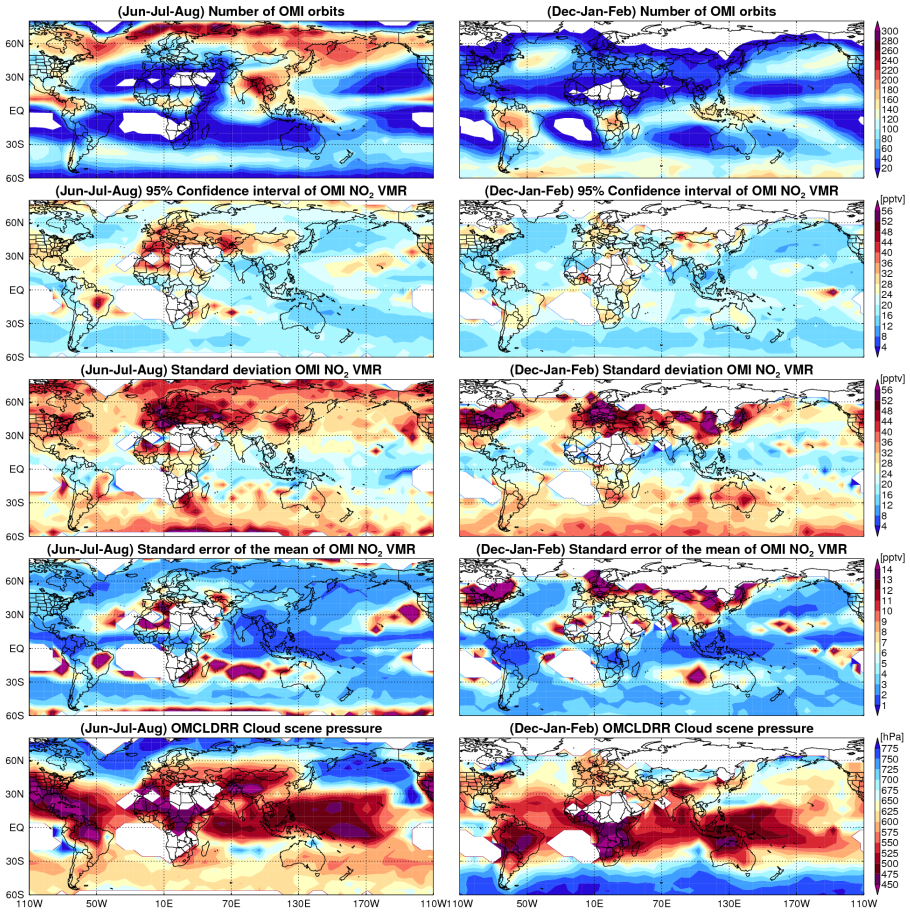

Fig. C1. Left: June–August and right: December–February averages over 2005–2007: first row: number of OMI overpasses used to derive NO_2 VMR climatology; second row: 95 % confidence interval of NO_2 VMRs; third row: standard deviation of NO_2 VMRs; fourth row: standard error of the mean of NO_2 VMRs; fifth row: mean OMCLDRR cloud scene pressures used to compute the NO_2 VMR climatology.

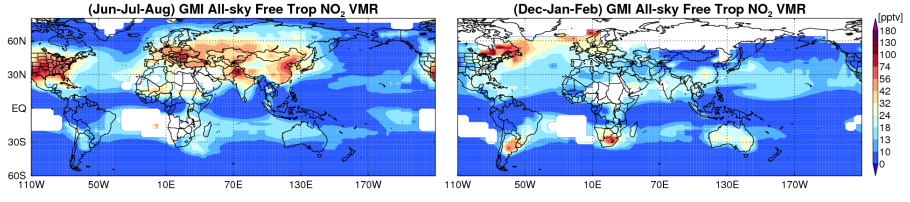

Fig. C2. GMI all-sky free tropospheric NO_2 for June–August (left) and December–February (right) averages over 2005–2007.

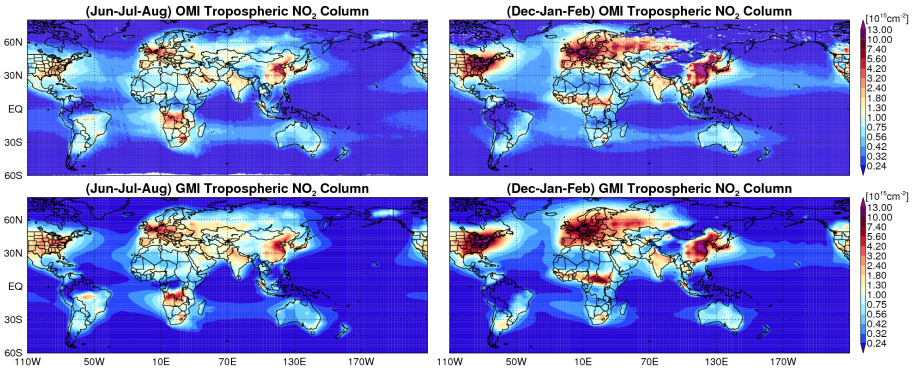

Fig. C3. For June–August (left column) and December–February (right column) averages over 2005–2007; top: OMI tropospheric column NO_2; bottom: GMI tropospheric column NO_2.

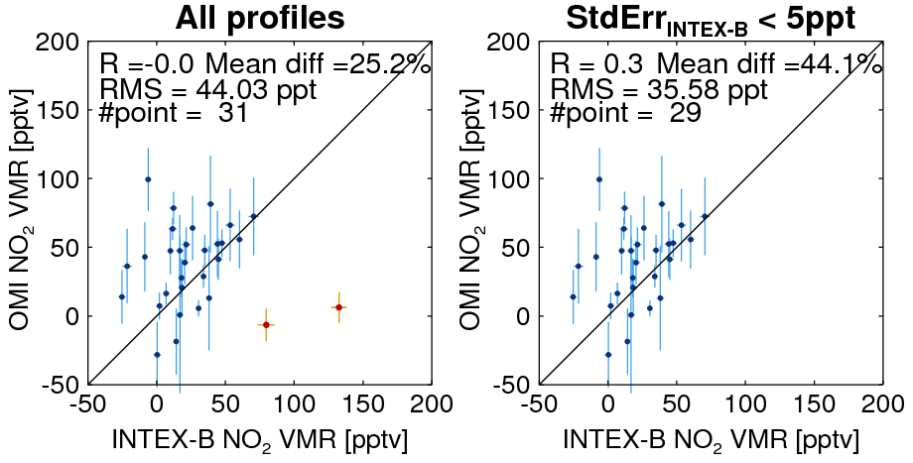

Fig. D1. Similar to Fig. 6 but using geometric AMF.

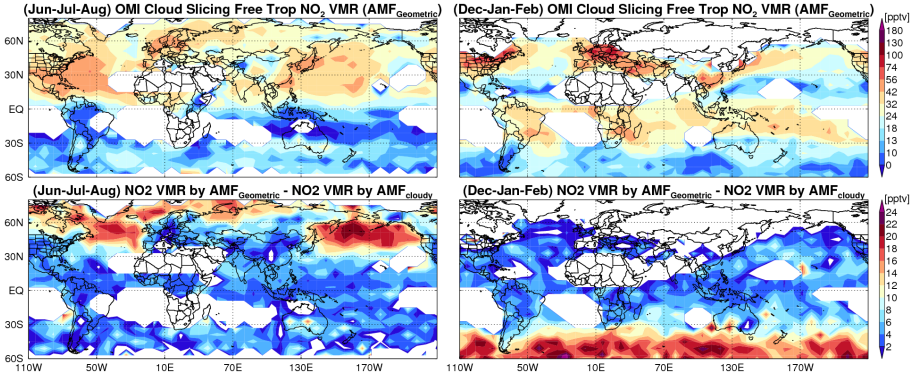

Fig. D2. For June–August (left) and December–February (right) averaged over 2005–2007, top: global maps of NO_2 VMR calculated using geometric AMFs; bottom: difference in NO_2 VMRs computed using geometric and near-Lambertian AMFs.

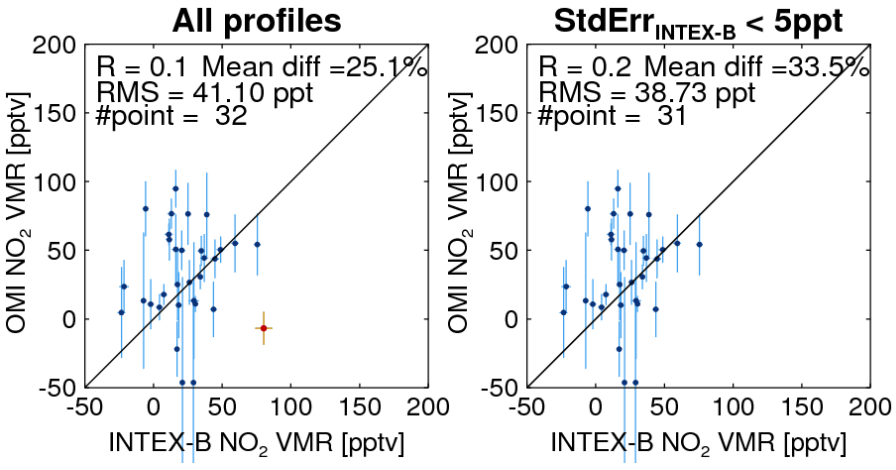

Fig. D3. Similar to Fig. 6 but using OMCLDO2 data and geometric AMF.

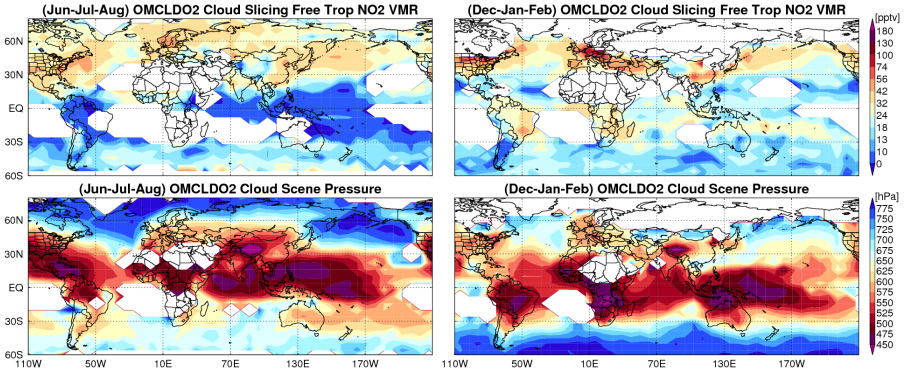

Fig. D4. For June–August (left) and December–February (right) averaged over 2005–2007, top: global maps of NO_2 VMR calculated using geometric AMFs and OMCLDO2 cloud parameters; bottom: mean cloud scene pressures from OMCLDO2.